

AD-A061 208

PENNSYLVANIA STATE UNIV UNIVERSITY PARK APPLIED RESE--ETC F/G 20/4  
A METHOD FOR CALCULATING THE FLOWFIELD IN THE TAIL REGION OF A --ETC(U)  
JUL 78 G H HOFFMAN N00017-73-C-1418

UNCLASSIFIED

ARL/PSU/TM-78-211

NL

| OF |

AD  
A061208



END  
DATE  
FILMED

2 - 75  
DDC

AD A061208

LEVEL

12

A METHOD FOR CALCULATING THE FLOWFIELD IN THE TAIL REGION OF A BODY OF REVOLUTION

G. H. Hoffman

DDC FILE COPY

DDC  
NOV 15 1978  
F

Technical Memorandum  
File No. TM 78-211  
July 19, 1978  
Contract No. N00017-73-C-1418

Copy No. 46

The Pennsylvania State University  
Institute for Science and Engineering  
APPLIED RESEARCH LABORATORY ✓  
Post Office Box 30  
~~State College, Pa. 16801~~ University Park.

NAVY DEPARTMENT  
NAVAL SEA SYSTEMS COMMAND

Approved for Public Release  
Distribution Unlimited

78 11 06 088

UNCLASSIFIED

9 Technical memo.

SECURITY CLASSIFICATION OF THIS PAGE (When Data Entered)

REPORT DOCUMENTATION PAGE		READ INSTRUCTIONS BEFORE COMPLETING FORM
1. REPORT NUMBER TM 78-211	2. GOVT ACCESSION NO. 14/ARL/PSTU/TM-78-211	3. RECIPIENT'S CATALOG NUMBER
4. TITLE (and Subtitle) A METHOD FOR CALCULATING THE FLOWFIELD IN THE TAIL REGION OF A BODY OF REVOLUTION.		5. TYPE OF REPORT & PERIOD COVERED Technical Memorandum
7. AUTHOR(s) G. H. Hoffman		6. PERFORMING ORG. REPORT NUMBER
9. PERFORMING ORGANIZATION NAME AND ADDRESS Applied Research Laboratory P. O. Box 30 State College, PA 16801		8. CONTRACT OR GRANT NUMBER(s) N00017-73-C-1418
11. CONTROLLING OFFICE NAME AND ADDRESS Naval Sea Systems Command Washington, DC 20362		10. PROGRAM ELEMENT, PROJECT, TASK AREA & WORK UNIT NUMBERS
14. MONITORING AGENCY NAME & ADDRESS (if different from Controlling Office) 12/63p.		12. REPORT DATE 11/79 July 1978
		13. NUMBER OF PAGES 57
		15. SECURITY CLASS. (of this report) UNCLASSIFIED
		15a. DECLASSIFICATION/DOWNGRADING SCHEDULE
16. DISTRIBUTION STATEMENT (of this Report) Approved for Public Release. Distribution Unlimited. Per NAVSEA - Oct. 16, 1978.		
17. DISTRIBUTION STATEMENT (of the abstract entered in Block 20, if different from Report)		
18. SUPPLEMENTARY NOTES		
19. KEY WORDS (Continue on reverse side if necessary and identify by block number) hydrodynamics      calculation flow boundary layer streamline		
20. ABSTRACT (Continue on reverse side if necessary and identify by block number) (U) A method is presented for calculating a high Reynolds number flow field in the aft region of a body of revolution without appendages where the boundary layer and outer inviscid flow strongly interact. The method is based on a correction of the displacement body idea to effectively represent streamline curvature effects by means of a simple pressure mapping. The problem is solved numerically on a digital computer by iterating for the unknown displacement body surface. Typically, from 6 to 8 iterations are		

391 007

Handwritten signature

UNCLASSIFIED

SECURITY CLASSIFICATION OF THIS PAGE(When Data Entered)

required for convergence. Available computation codes are used for the boundary layer flow and outer inviscid flow while a simple integral model is used for the wake. Comparisons of computed results are made with experiment and other numerical solutions for three bodies.

UNCLASSIFIED

SECURITY CLASSIFICATION OF THIS PAGE(When Data Entered)

**Subject:** A Method for Calculating the Flowfield in the Tail Region of a Body of Revolution

**References:** See Page 33

**Abstract:** A method is presented for calculating a high Reynolds number flow field in the aft region of a body of revolution without appendages where the boundary layer and outer inviscid flow strongly interact. The method is based on a correction of the displacement body idea to effectively represent streamline curvature effects by means of a simple pressure mapping. The problem is solved numerically on a digital computer by iterating for the unknown displacement body surface. Typically, from 6 to 8 iterations are required for convergence. Available computation codes are used for the boundary layer flow and outer inviscid flow while a simple integral model is used for the wake. Comparisons of computed results are made with experiment and other numerical solutions for three bodies.

**Acknowledgement:** This work was sponsored by Naval Sea Systems Command, Codes NSEA-0351 and NSEA-03133.

ACCESSION for	
NTIS	White Section <input checked="" type="checkbox"/>
DDC	Buff Section <input type="checkbox"/>
UNANNOUNCED	<input type="checkbox"/>
JUSTIFICATION	
BY	
DISTRIBUTION/AVAILABILITY CODES	
Dist.	SPECIAL
A	

Table of Contents		<u>Page</u>
Abstract . . . . .		1
Acknowledgement . . . . .		1
Nomenclature . . . . .		3
List of Figures . . . . .		5
List of Tables . . . . .		7
Introduction . . . . .		8
Pressure Mapping Hypothesis . . . . .		10
Strong Interaction Calculation Method . . . . .		14
Wake Model . . . . .		17
Calculated Results . . . . .		21
Lyon Model A Body . . . . .		23
Modified Spheroid . . . . .		25
F-57 Body . . . . .		27
Conclusions . . . . .		30
References . . . . .		33
Figures . . . . .		35

## Nomenclature

$A_0$	reference area
$C_D$	drag coefficient ( $= \text{drag} / \frac{1}{2} \rho U_\infty^2 A_0$ )
$C_f$	wall friction coefficient ( $= \tau_w / \frac{1}{2} \rho u_e^2$ )
$C_p$	pressure coefficient
H	axisymmetric shape factor
L	body length
n	distance normal to stream surface
p	static pressure
q	velocity along streamline
r	radial distance
$r_0$	local body radius
R	radius of curvature
$Re$	Reynolds number ( $= U_\infty L / \nu$ )
s	distance along stream surface
u	velocity in x-direction
$u_e$	inviscid velocity at $r = r_0$
$U_\infty$	free stream velocity
x	distance along body surface
$x_0$	axial distance
y	distance normal to body surface
$\delta$	boundary-layer thickness
$\delta_1^*$	axisymmetric physical displacement thickness
$\Delta^*$	mass deficit area ( $= \int_0^\infty (1 - \frac{u}{u_e}) r dy$ )
$\epsilon$	eddy viscosity
$\nu$	kinematic viscosity

Nomenclature (Cont.)

$\phi$	angle between tangent to body surface and $x_0$ -direction
$\rho$	density
$\Theta$	momentum deficit area ( $= \int_0^{\infty} \frac{u}{u_e} (1 - \frac{u}{u_e}) r dy$ )
$\tau_w$	surface shear stress

All other quantities and subscripts are defined in the text.

All quantities in the text (unless otherwise specified) are made dimensionless as follows:

- distance with respect to  $L$
- area with respect to  $L^2$
- velocity with respect to  $U_{\infty}$
- pressure with respect to  $\rho U_{\infty}^2$

List of Figures

<u>Figure</u>		<u>Page</u>
1	Displacement Body Geometry . . . . .	35
2-8	<u>Lyon Model A Body</u> . . . . .	
2	Body Geometry . . . . .	36
3	Body Pressure Distribution . . . . .	37
4	Momentum Deficit Area . . . . .	38
5	Wall Friction Coefficient . . . . .	39
6	Boundary-Layer Shape Factor . . . . .	40
7	Mean Velocity Profile, $x_0 = 0.60$ . . . . .	41
8	Mean Velocity Profile, $x_0 = 0.90$ . . . . .	42
9-15	<u>Modified Spheroid</u> . . . . .	
9	Body Geometry . . . . .	43
10	Body Pressure Distribution . . . . .	44
11	Momentum Deficit Area . . . . .	45
12	Wall Friction Coefficient . . . . .	46
13	Boundary-Layer Shape Factor . . . . .	47
14	Mean Velocity Profile, $x_0 = 0.662$ . . . . .	48
15	Mean Velocity Profile, $x_0 = 0.960$ . . . . .	49
16-23	<u>F-57 Body</u> . . . . .	
16	Body Geometry . . . . .	50
17	Body Pressure Distribution . . . . .	51
18	Momentun Deficit Area . . . . .	52
19	Wall Friction Coefficient . . . . .	53
20	Boundary-Layer Shape Factor . . . . .	54
21	Mean Velocity Profile, $x_0 = 0.601$ . . . . .	55

List of Figures (Cont.)

<u>Figure</u>		<u>Page</u>
22	Mean Velocity Profile, $x_0 = 0.880$ . . . . .	56
23	Mean Velocity Profile, $x_0 = 0.990$ . . . . .	57

List of Tables

<u>Table</u>		<u>Page</u>
1	Drag Coefficient for Lyon Model A Body . . . . .	24
2	Drag Coefficient for Modified Spheroid . . . . .	26
3	Variation of Wake Integral Parameters for F-57 Body . . . . .	28

Introduction

The most difficult part of the flow field to compute about a body of revolution is in the vicinity of the tail-wake juncture, referred to as the strong interaction region. For applications this region is important in two respects. First, the drag depends to a large extent on the flow in this region and second, when a propeller or other propulsive device is added it always operates in the thick boundary layer near the tail.

This report addresses the problem of calculating the flow field in the strong interaction region of a body of revolution at zero angle of attack where the boundary layer does not separate. The aim has been to develop an engineering tool capable of predicting this flow field with reasonable accuracy using a blend of available calculation methods plus a new twist to the displacement body idea. Only the incompressible case is considered.

The phenomenon that occurs in the tail-wake juncture region of a body of revolution can be explained as follows: Toward the aft end of a body with a pointed tail the boundary-layer thickness becomes comparable to the body radius thereby significantly displacing the streamlines of the outer inviscid flow which in turn modifies the body pressure distribution. In addition, the streamlines of the outer flow, sensing the wake line of symmetry approaching, undergo a significant change in direction over a relatively short distance thereby impressing a non-negligible normal pressure gradient on the boundary layer. To treat the resulting strong interaction, the equations governing the boundary layer and the outer flow need to be solved simultaneously and the assumptions of conventional boundary-layer theory modified.

Over the past 10 to 15 years a number of methods have appeared for solving the strong interaction problem. The most common method is the displacement body approach, the category under which the present work falls. In this method the boundary-layer displacement thickness is added to the original body to represent the thickening effect that the outer flow senses and the boundary layer calculated as though no normal pressure gradient existed. The new aspect of the present work is that the displacement body idea is modified by a simple pressure mapping which effectively represents streamline curvature effects on the boundary layer.

A comprehensive review up to 1976 on methods of treating the strong interaction problem has been given by Huang et. al. [1]. Since that time two other papers dealing with new approaches to the problem have appeared. The work by Schetz and Favin [2] is the most exact approach to the problem to date. They numerically solve the Navier-Stokes equations with a one equation transport-type turbulence model in a truncated region which includes the aft portion of the body and part of the wake. The effect of a propeller positioned at the tail is modeled by an actuator disk. Unfortunately no comparison with experiment is given. The recent paper by Dyne [3] is a streamline curvature method in which the effects of turbulence in the boundary layer have been accounted for approximately. The calculation region where the streamline curvature method is applied is the aft portion of the body and the near wake, similar to the computational region of Schetz and Favin. The virtue of the streamline curvature method is that the normal pressure gradient caused by streamline curvature is taken into account while the simplicity of a boundary layer-like formulation is retained. Agreement with experiment for the one case presented, a modified spheroid, is good.

## 2. Pressure Mapping Hypothesis

In the usual displacement body treatment, the pressure from that body is referred back to the original body along a boundary-layer normal coordinate. As Weinbaum et al. [4] point out, this transfer implies that the pressure gradients on the two bodies are related by

$$\frac{dp}{ds_w} = \frac{R^*}{R_w} \frac{dp}{ds^*}, \quad (1)$$

where the subscript  $w$  denotes the surface of the original body, the superscript  $*$  the surface of the displacement body,  $s$  is arc length and  $R$  is the local radius of curvature. Equation (1) is a consequence of the differential arc length relation between the displacement body and the original body,

$$\frac{R^*}{R_w} ds_w = ds^*, \quad (2)$$

which holds provided the bodies are sufficiently smooth and the curvatures are changing slowly.

The two-dimensional analysis of Weinbaum et al. for a thick viscous layer at intermediate Reynolds numbers will now be extended to the axisymmetric case at high Reynolds numbers. The object of this analysis is to determine how the conventional displacement body idea must be modified to account for centrifugal effects in a turbulent wall shear layer at high Reynolds numbers. With the assumption that the turbulence field can be modeled by an eddy viscosity, the appropriate set of equations in mean flow intrinsic coordinates is,

$$q \frac{\partial q}{\partial s} = - \frac{\partial p}{\partial s} + \frac{1}{Re r} \frac{\partial}{\partial n} [(1+\epsilon)r \frac{\partial q}{\partial n}], \quad (3)$$

$$\frac{q^2}{R} = \frac{\partial p}{\partial n}. \quad (4)$$

These equations are the axisymmetric turbulent analogs of Eqs. (2) and (3) of Weinbaum et al. The above equations have been made dimensionless with velocities referred to free stream velocity  $U_\infty$ , pressure to  $\rho U_\infty^2$ , lengths to reference length  $L$  and eddy viscosity to kinematic viscosity  $\nu$ . Equations (3) and (4) are derived by considering the full axisymmetric Navier-Stokes equations in general orthogonal coordinates, introducing the usual Reynolds turbulence averaging, making the boundary-layer approximation and finally, specializing the result to intrinsic coordinates of the mean turbulent flow.

Equations (3) and (4) are now ordered in terms of the Reynolds number by stretching the normal coordinate according to the usual high Reynolds number boundary-layer scaling:

$$n = \frac{\bar{n}}{Re^{1/2}}. \quad (5)$$

In the intermediate Reynolds number case of Weinbaum et al. both spatial variables are scaled by the inverse square root of the Reynolds number. With the scaling given by Eq. (5) the equations of the thick shear layer become

$$q \frac{\partial q}{\partial s} = - \frac{\partial p}{\partial s} + \frac{1}{r} \frac{\partial}{\partial \bar{n}} [(1+\epsilon)r \frac{\partial q}{\partial \bar{n}}], \quad (6)$$

$$\frac{q^2}{R} = Re^{1/2} \frac{\partial p}{\partial \bar{n}}. \quad (7)$$

The convective acceleration term is eliminated by differentiating Eq. (7) with respect to  $s$ , then substituting the result into Eq. (6) which gives the following equation:

$$\frac{\partial}{\partial \bar{n}} \left( \frac{\partial p}{\partial s} \right) + \frac{1}{Re^{1/2} R} \frac{\partial p}{\partial s} = - \frac{1}{Re^{1/2}} \left( \frac{q}{R} \right)^2 \frac{\partial R}{\partial s} + \frac{2}{Re^{1/2} R r} \frac{\partial}{\partial \bar{n}} [(1+\epsilon)r \frac{\partial q}{\partial \bar{n}}]. \quad (8)$$

Note that Eq. (8) is the high Reynolds number axisymmetric analog of Eq. (5) of Weinbaum et al. and describes the variation of streamwise pressure gradient across the shear layer.

To simplify the integration of the left-hand side of Eq. (8) the local radius of curvature is approximated by

$$R = R_w + \frac{\bar{n}}{Re^{1/2}}. \quad (9)$$

Then integration of Eq. (8) from the wall ( $\bar{n} = 0$ ) to a point in the shear layer gives the streamwise pressure gradient at  $\bar{n}$  as

$$\frac{\partial p}{\partial s} = \left(\frac{R_w}{R}\right)^2 \left(\frac{\partial p}{\partial s}\right)_w - \frac{1}{Re^{1/2}} \left\{ \frac{1}{R^2} \left(\frac{dR}{ds}\right)_w \int_0^{\bar{n}} q^2 d\bar{n} - \frac{2}{R^2} \int_0^{\bar{n}} \frac{R}{r} \frac{\partial}{\partial \bar{n}} \left[ (1+\epsilon) r \frac{\partial q}{\partial \bar{n}} \right] d\bar{n} \right\}. \quad (10)$$

Equation (10) shows that the change in streamwise pressure gradient normal to the wall is dominated by streamline curvature effects, represented by the first term. The remaining terms,  $O(Re^{-1/2})$ , represent respectively changes due to streamwise variation in wall curvature and laminar/turbulent diffusion.

One next applies Eq. (10) at the surface of the displacement body, assuming that body to be a streamline of the actual flow (which in reality it is not). Thus the streamwise pressure gradient along the displacement body is

$$\frac{\partial p}{\partial s^*} = \left(\frac{R_w}{R^*}\right)^2 \left(\frac{\partial p}{\partial s}\right)_w + O(Re^{-1/2}). \quad (11)$$

The pressure gradient on the displacement body is now transferred back to the original body along the boundary-layer normal according to Eq. (1) which gives the result

$$\left(\frac{\partial p}{\partial s}\right)_{w\bar{n}} = \left(\frac{R^*}{R_w}\right) \left(\frac{\partial p}{\partial s}\right)_w + O(Re^{-1/2}), \quad (12)$$

where the subscript  $\bar{w}$  denotes the wall pressure gradient in the presence of a normal pressure field. If the following arc length stretching is now defined:

$$ds_w = \left(\frac{R^*}{R_w}\right) ds_{\bar{w}} = ds^*, \quad (13)$$

then Eq. (12) becomes

$$\frac{\partial p}{\partial s^*} = \left(\frac{\partial p}{\partial s}\right)_w + O(\text{Re}^{-1/2}), \quad (14)$$

which is the result obtained by Weinbaum et al. Equations (13) and (14) are the essence of Weinbaum's hypothesis which states: "The pressure gradient along the displacement body constructed in the conventional manner using first-order boundary-layer theory will be the same as in a viscous/turbulent shear layer theory which includes centrifugal effects provided the pressure on the displacement body is referred back to the original body in a manner that preserves the arc length." The present analysis shows that Weinbaum's hypothesis is unchanged by either axial symmetry or a turbulent eddy viscosity.

In regions of large changes in the streamline curvature both neglected terms in Eq. (10) may become  $O(1)$  which will invalidate Weinbaum's hypothesis. In the high Reynolds number case the diffusion term becomes equal in importance to the term arising from streamwise variations in the wall curvature, in contrast to the intermediate Reynolds number case where the diffusion term is  $O(\text{Re}^{-1})$ . This behavior is a consequence of the different scalings.

The crucial assumption in the preceding development and the one directly responsible for the simple form of Weinbaum's hypothesis is Eq. (9), the approximation of the local radius of curvature. Physically this approximation means that the streamlines are locally concentric which is usually not the case near the tail of the body. The validity of Weinbaum's hypothesis with its simplifying assumptions can only be determined by comparison with experiment over a range of strong interaction cases.

### 3. Strong Interaction Calculation Method

The solution for the location of the displacement body requires that the inviscid pressure distribution be known at the surface of the original body. In turn, the solution for the pressure distribution on the original body requires that the displacement body be known. Thus a coupled nonlinear boundary value problem exists which must be solved by iteration.

The iteration procedure used here follows closely the schemes used in displacement body calculations found in the literature [1, 5, 6]. The general steps in the iteration are as follows:

#### First iteration

1. Compute the inviscid pressure distribution for the basic body.
2. Modify the pressure distribution from step 1 on the afterbody to eliminate the rear stagnation point, if it exists, so that boundary-layer separation will be avoided. Guess the wake pressure distribution for  $1 \leq x_0 \leq 2$ . Step 2 gives the first approximation of the pressure distribution over the body-wake combination.
3. With the pressure distribution from step 2 compute the boundary layer along the actual body and the wake at least one body length downstream of the tail. This step gives the first approximation to the displacement body.

#### Second and succeeding iterations

1. Compute the inviscid pressure distribution using the displacement body from the last step of the previous iteration.
2. Transfer the pressure distribution from the displacement body back to the basic body and the wake centerline, preserving arc length (Weinbaum's hypothesis).

3. With the pressure distribution from step 2, compute the boundary layer along the actual body and the wake to obtain a new estimate of the displacement body shape.

The iteration cycle is continued until convergence is achieved. The pressure, being the most sensitive variable, is monitored until its maximum change over successive iterations is sufficiently small. The steps as outlined above will be elaborated upon as each part of the calculation cycle is taken up in detail. What distinguishes the present displacement body method from others is the use of Weinbaum's hypothesis to account for centrifugal effects.

The philosophy followed here has been to use available calculation methods as much as possible for the components of the strong interaction calculation - the inviscid flow, the boundary layer and the wake. For the inviscid flow the method of Hess and Smith [7] is used. For the boundary-layer calculation transverse curvature terms are included in the equations (the so-called thick boundary-layer approximation). These equations are solved by a modified Cebici-Smith finite difference approach [8] which makes use of the second-order accurate form of Keller's box method. The code in use was generated at ARL and includes a two-layer algebraic turbulence model composed of the Cebici form for the outer eddy viscosity [8] and the Crawford-Kays form for the inner eddy viscosity [9]. The inner eddy viscosity has been modified for a thick axisymmetric boundary layer and reformulated to work properly in the region of a pointed tail. For the wake calculation an integral method is used which is covered in detail in the next section.

In the axisymmetric boundary layer three definitions of the displacement

thickness exist. The one appropriate to the displacement body is the so-called physical definition  $\delta_1^*$  which is derived from the mass flow defect in the annular boundary layer wrapped around the body:

$$\int_{r_0}^{r_0 + \delta_1^* \cos \phi} 2\pi r u_e dr = \int_{r_0}^{r_0 + \delta \cos \phi} 2\pi r (u_e - u) dr.$$

Integration of the above equation with the aid of the geometric relation  $r = r_0 + y \cos \phi$  in the right-hand integral yields

$$\delta_1^* r + \frac{1}{2} \delta_1^{*2} \cos \phi = \int_0^\delta \left(1 - \frac{u}{u_e}\right) r dy = \Delta^*, \quad (15)$$

where  $\Delta^*$  is the mass deficit area. From Eq. (15) the solution for  $\delta_1^*$  is

$$\delta_1^* = \frac{(2\Delta^* \cos \phi + r_0^2)^{\frac{1}{2}} - r_0}{\cos \phi} \quad (16)$$

From the geometry shown in Fig. 1 the coordinates of the displacement body are given by:

$$(r_0)_{\delta^*} = r_0 + \delta_1^* \cos \phi,$$

$$(x_0)_{\delta^*} = x_0 - \delta_1^* \sin \phi,$$

or finally,

$$(r_0)_{\delta^*} = (2\Delta^* \cos \phi + r_0^2)^{\frac{1}{2}}, \quad (17)$$

$$(x_0)_{\delta^*} = x_0 - \tan \phi [(2\Delta^* \cos \phi + r_0^2)^{\frac{1}{2}} - r_0]. \quad (18)$$

#### 4. Wake Model

Because of the presence of a wake the displacement body continues to infinity downstream of the end of the actual body, but its importance aft of the tail in establishing curvature effects on the body pressure distribution is mainly in the near wake region ( $1.0 \leq x_0 \leq 1.1$ ). Thus the wake portion of the displacement body must be included in a strong interaction calculation but the calculation of the wake can be terminated about one body length downstream of the tail without producing any adverse effects in the overall solution.

The wake is modeled in the simplest manner possible by using an integral approach. The two variations in this type of treatment involve either using an entrainment relation, as in the work of Nakayama, Patel and Landweber [10], or using a relation between shape factor and inviscid velocity, as in the work of Granville [11]. Granville's variant was chosen because it leads to a simple closed form solution whereas the entrainment method must be integrated numerically. Furthermore, as Patel and Guven point out [12], the assumed variation of  $H$  with  $u_e$  is not crucial to the determination of the asymptotic wake behavior. But, as will be seen, the asymptotic behavior does strongly depend on the initial values of  $u_e$  and  $\theta$ .

In the wake the axisymmetric integral momentum equation with normal pressure variations neglected reduces to

$$\frac{d\theta}{dx} + (H+2) \theta \frac{d \ln u_e}{dx} = 0, \quad (19)$$

which can be written equivalently in the nearly integrable form:

$$\frac{d \ln \theta}{d \ln u_e} = - (H+2) \quad (20)$$

By curve fitting axisymmetric wake data Granville finds the following relation between  $H$  and  $u_e$  [11]:

$$H = 1 + (H_t - 1) \left( \frac{\ln u_e}{\ln u_{e_t}} \right)^{1/q} \quad (21)$$

where the subscript  $t$  denotes the tail of the body,  $x_0 = 1$ , and  $q$  is found by Granville to be 7. With the aid of Eq. (21), Eq. (20) can be integrated giving the result

$$\theta = \theta_\infty u_e^\beta, \quad (22)$$

where

$$\beta = \frac{2q + 3 + qH}{1 + q}, \quad (23)$$

and  $\theta_\infty$  is the momentum deficit area infinitely far downstream in the wake. In the present context  $u_e$  in Eq. (22) is the inviscid velocity on the wake centerline obtained by transferring the pressure on the displacement body to the wake centerline using Weinbaum's hypothesis.

Since we assume that Eq. (22) holds at the initial wake station, we can determine  $\theta_\infty$  in terms of  $\theta_t$ , known from the boundary-layer calculation at the tail, and  $u_{e_t}$ , known from the pressure mapping. Thus

$$\theta_\infty = \theta_t u_{e_t}^\beta, \quad (24)$$

and hence at any other station in the wake  $\theta$  is given by Eq. (22) and  $H$  by Eq. (21). Note that Eq. (24) is the expression from which Granville's drag formula is derived.

With  $\theta$  and  $H$  known at a particular wake station, the displacement area  $\Delta^*$  is given by

$$\Delta^* = H\theta, \quad (25)$$

and finally, the radius of the displacement body is given by Eq. (17)

which in the wake reduces to

$$(r_0)_{\delta^*} = (2\Delta^*)^{\frac{1}{2}}. \quad (26)$$

The initial values of the wake parameters to be used in Eq. (24) are obtained by requiring  $r_{\delta^*}$  and  $H$  to be continuous at the body-wake juncture. Obviously the displacement body radius must be continuous for a smooth pressure distribution to exist. The requirement of continuous  $H$  is based on the observation that a non-zero tail angle, which causes a mismatch or overlap in boundary-layer coordinates with wake (cylindrical) coordinates, does not appear to introduce a discontinuity in the measured shape factor. These two conditions are sufficient to determine the remaining parameters at the body-wake juncture. With  $r_{\delta^*}$  and  $H$  known at the initial wake station  $t$ , and with  $u_{e_t}$  given by the pressure mapping, the other parameters are given by:

$$\Delta^*_t = \frac{1}{2} (r_{\delta^*_t})^2, \quad (27)$$

and

$$\theta_t = \frac{\Delta^*_t}{H_t} \quad (28)$$

Although  $r_{\delta^*}$  and  $H$  are forced to be continuous at  $x_0 = 1.0$ , the other parameters at that point may be discontinuous since a finite difference boundary-layer solution is being joined to an integral wake solution. These discontinuities have been found to be quite small. Other ways of treating the boundary layer-wake juncture were tried but none gave as satisfactory results as the simple treatment just described.

The Mangler transformation used in the Cebici-Smith boundary-layer method introduces a singularity into the equations of motion at the tail

when the body radius there is zero. Consequently the boundary layer solution cannot be calculated all the way to the tail with this method. This difficulty is overcome by computing the boundary-layer solution to about  $x_0 = 0.99$ , then obtaining values of  $r_{\delta^*}$  and  $H$  at the tail station by parabolic extrapolation.

### 5. Calculated Results

To begin a strong interaction calculation, the body pressure distribution obtained by solving the potential flow problem about the basic body without a displacement thickness added is modified in the tail region to approximate the converged strong interaction solution. The modified pressure distribution is then extrapolated into the wake. The modification of the basic pressure distribution begins at about  $x_0 = 0.85$  with the modified curve passing smoothly through  $C_p = 0.2$  at  $x_0 = 1.0$ , then decaying rapidly to zero in the wake. The wake  $C_p$  distribution is approximated by

$$C_p = 0.2 \operatorname{sech} [20.6(x_0 - 1)], \quad x_0 \geq 1. \quad (29)$$

Even though the initial guess is a reasonably good one the second iteration usually produces an overcorrection to the pressure distribution which if carried further leads to divergence. This type of behavior was also found by Nakayama et al. [10]. Their solution to the overcorrection problem was to compute a pressure distribution for the second iteration by averaging the initial guess (first iteration) and the pressure distribution obtained from the resulting first iteration boundary-layer solution. After the second iteration, averaging was found to be unnecessary and a convergent procedure followed. This same procedure was found to work successfully in the present calculation method. The only difference is that here the averaging is performed after the application of the pressure mapping.

During the initial stages of this work convergence was found to be slowest in the region near the tail-wake juncture because spurious jumps in the pressure distribution occurred. These jumps were found to be

caused by discontinuities in the slope and curvature of the displacement body at the juncture point which in turn stemmed from the incompatibility of a finite difference boundary layer solution patched to an integral wake solution.

Huang et al. [1], whose strong interaction calculation method the present one resembles, also encountered spurious pressure jumps in the tail-wake juncture region where they represented the displacement body by a polynomial between  $0.95 < x_0 < 1.05$ . When a fifth-order polynomial was used to ensure continuity of radius, slope and curvature at the juncture points the pressure jumps disappeared. Their polynomial fairing thus provided a smoothing of the pressure in the tail-wake juncture region.

Smoothing in the present calculations was performed when needed by fairing out the spurious jumps in the pressure distribution by hand rather than fairing the displacement body tail-wake juncture. Although the present method of eliminating the pressure jumps is primitive and involves judgement on the part of the user, the iteration process does converge, usually within 6 to 8 iterations, and the pressure jumps disappear by the final iteration. Convergence is considered achieved when the maximum change in  $u_e$  (rather than  $C_p$ ) is less than about one percent. The maximum change always occurs close to the tail-wake juncture.

Present experience with the Cebici-Smith boundary-layer calculation method shows that even though the sublayer-buffer region of the turbulent boundary layer may be adequately resolved at, say,  $x_0 = 0.95$ , it will not be at  $x_0 = 0.99$ . The fault lies with the Mangler transformation which is singular at the tail when body radius is zero. The step size problem may be demonstrated as follows: For the first step normal to the body in the

boundary layer the physical step size  $\Delta y_1$  is related to the transformed step size  $\Delta \eta_1$  by (see Ref. 8, p. 260)

$$\Delta y_1 = \text{constant} \times \frac{\Delta \eta_1}{r_0}$$

so that as  $r_0 \rightarrow 0$  with  $\Delta \eta_1$  fixed, the physical step size in the boundary layer becomes large even though  $\Delta \eta_1$  may be extremely small.

Solutions were computed by the present method for three axisymmetric bodies for which experimental data have been published. The three cases are the model A body of Lyon [13], a modified spheroid [14] and a low-drag body [15]. The first two bodies have non-zero tail angles while the last is nearly cusped. In each case comparisons with the data are given for body pressure coefficient  $C_p$ , momentum deficit area  $\Theta$ , shape factor  $H$  and skin friction coefficient  $C_f$  plus selected velocity profiles. Where possible comparisons are also made with published theoretical results.

#### Lyon Model A Body

Calculations were made at a body chord Reynolds number of  $2.09 \times 10^6$ , the same as in Lyons' experiments [13]. The transition location in the calculation was adjusted so that  $\Theta$  in the laminar-turbulent region ( $0.1 < x_0 < 0.4$ ) closely fitted the experimental data given in Fig. 24 of ref. 13. These data correspond to the case with a screen ahead of the model. The turbulent eddy viscosity in the calculation is activated gradually downstream of the transition station by using the intermittency factor of Chen and Thyson [16].

The geometry of the Lyon model A body is shown in Fig. 2. Figure 3 presents a comparison between the calculated and measured pressure distributions on the aft portion of the body. The calculated pressure distribution

along the wake centerline is also shown where no measurements were made. In addition, the potential solution (no boundary-layer interaction) and the strong interaction solution of Nakayama, Patel and Landweber [10] are presented for comparison. The agreement of the solution of Nakayama et al. with the data is slightly better than the present solution. In Fig. 4 the momentum deficit area distribution as predicted by the present method and that of Nakayama et al. is compared with the experimental data. On the body both predictions agree closely with experiment. In the wake the calculated values of Nakayama et al. are above those of the present method.

Since a strong interaction calculation necessarily includes the wake, one of the results is the body drag which is related to the momentum area at downstream infinity by

$$C_D = \frac{4\pi}{A_0} \Theta_\infty$$

where  $A_0$  is the reference area. A comparison between experiment and several calculations of  $C_D$  (based on body surface area) for the Lyon model A body is given in Table 1.

Source	$C_D$
Experiment - Lyon [13]	.00436
Present calculation	.00401
Calculation - Nakayama et al. [10]	.00410
Calculation - Myring [5]	.00397

Table 1. Drag Coefficient for Lyon Model A Body.

The spread in the three calculated values is only 3.2 percent.

The results for  $C_f$  and  $H$  are shown in Figs. 5 and 6 respectively. Lyons' measured values of  $C_f$  display an erroneous trend near the tail of the body but agree well with the present calculation over the front portion.

The shape factor is predicted better over the last 30 percent of the body by the integral method of Nakayama et al. than the present finite difference method. The reason for the poor showing of the present method for  $H$  is attributed to inadequacy of the algebraic turbulence model in the tail region even though transverse curvature effects are included in the model as well as in the boundary-layer equations. Velocity profiles are shown at  $x_0 = 0.6$  in Fig. 7, where the thin boundary-layer approximation is valid, and at  $x_0 = 0.9$  in Fig. 8 in the strong interaction region where transverse curvature effects are important. At  $x_0 = 0.6$  agreement with experiment is excellent but at  $x_0 = 0.9$  the shape of the predicted profile is too full near the surface. The latter behavior is typical of the present method for the three cases presented herein.

#### Modified Spheroid

The body used by Patel, Nakayama and Damian [14] in their experiments was a spheroid of approximately 6:1 fineness ratio with the rear 7 percent removed and a tangent cone added to prevent boundary-layer separation. The modified spheroid geometry is shown in Fig. 9. Corresponding to the experiment of Patel et al., strong interaction calculations have been made at a chord Reynolds number of  $1.262 \times 10^6$  and the eddy viscosity switched on at  $x_0 \approx 0.05$  to simulate the boundary-layer trip on the actual body. Comparisons between present calculations, those of Nakayama et al. [10] and the experiments of Patel et al. are given in Figs. 10 - 15. The pressure distribution on the body and on the wake centerline as well as the momentum deficit area distribution, shown in Figs. 10 and 11 respectively, are predicted well by both methods except that the calculated pressure peak near the tail is slightly high. Note that for this body the departure

from the potential flow pressure distribution begins at  $x_0 \approx 0.70$ . For both sets of calculations the skin friction coefficient is generally higher than the experimental values as seen in Fig. 12. The present calculation indicates that the boundary-layer nearly separates at  $x_0 = 0.94$  but then recovers. This trend is not shown by the integral method result of Nakayama et al.

The boundary-layer shape factor prediction by the present method, shown in Fig. 13, becomes increasingly less accurate as the tail is approached, as occurred for the Lyon body. The integral method calculation of Nakayama et al, is closer to the experimental values in the vicinity of the tail but in the wake the present method gives a better prediction of H. Nakayama et al. point out concerning their calculations for the modified spheroid that lower values of H and higher values of  $C_f$  have a mutually cancelling effect in the momentum equation in an adverse pressure gradient which explains why their method as well as the present one predict the momentum deficit area well near the tail.

The predicted velocity profiles for the modified spheroid, shown in Figs. 14 and 15, behave in much the same way as for the Lyon body. At  $x_0 = 0.662$  the prediction agrees well with experiment but at  $x_0 = 0.96$ , in the strong interaction region, the predicted velocities are too high near the wall.

Finally, the experimental and calculated drag coefficients for the modified spheroid are given in Table 2.

Source	$C_D$
Experiment - Patel et al. [15]	.00447 (average)
Present Calculation	.00454
Calculation - Nakayama et al. [10]	.00485
Calculation - Myring [6]	.00464

Table 2. Drag Coefficient for Modified Spheroid.

The present method gives the value closest to experiment.

Note that Patel and Guven [12] show that the use of Granville's wake formula, Eq. (24), leads to an overprediction of  $C_D$  for the spheroid of 30 percent where presumably they are using measured values of  $\theta$  and  $u_e$  at the tail station. The present prediction of  $C_D$  does not bear out their finding possibly because Weinbaum's hypothesis is used here to determine  $u_e$  at the tail and  $\theta_t$  is determined differently.

#### F-57 Body

The low drag F-57 body tested by Patel and Lee [15] is the last case considered. This body, shown in Fig. 16, has a nearly cusped tail so that the boundary layer on the aft end has a different history from the previous cases. The chord Reynolds number of the experiment was  $1.20 \times 10^6$  and the boundary layer was tripped at  $x_0 = 0.475$ , just ahead of where laminar separation would have occurred. Comparisons between present calculations, those of Patel and Lee [15] and experiment are shown in Figs. 17 - 23. The computed results of Patel and Lee, which are based on the integral boundary-layer method of Patel [17], used the measured pressure distribution at the edge of the boundary layer plus estimated values of the pressure integrals arising from variations normal to the streamlines. Integration of the equations was started at  $x_0 = 0.70$ . Hence the calculations of Patel and Lee are not a true strong interaction solution in which the pressure distribution is part of the solution.

As Fig. 17 shows, the present pressure distribution calculation agrees well with experiment both on the body and in the wake. As in previous cases the calculated result is slightly higher than experiment in the peak region near the tail. For this body comparison with the potential flow pressure distribution shows that the strong interaction region begins at  $x_0 \cong 0.75$ .

In computing the boundary-layer solution for the F-57 body, the station where the eddy viscosity is introduced was varied until agreement was obtained with the measured momentum deficit area in the trip region. As Fig. 18 shows, the calculated results for  $\theta$  by both methods agree well with experiment on the body but agreement becomes increasingly worse downstream in the wake. Consequently a question arises as to the source of the discrepancy between calculation and experiment for  $\theta$  in the wake. Estimates by Patel and Lee (see their Fig. 26) indicate that the pressure integral  $I_p$  arising from streamline curvature is practically negligible beyond the near wake ( $x_0$  greater than about 1.04). Hence the wake momentum integral equation, Eq. (19), should adequately represent the variation of  $\theta$ , especially if the measured values of  $H$  and  $u_e$  (corresponding to  $C_p$  on the wake centerline) are used. Such a calculation was made by numerically integrating Eq. (19) beginning from measured values at  $x_0 = 1.04$ . The results, shown in Table 3, are practically the same as the present strong interaction solution indicating that the experimental values of  $\theta$  in the wake by Patel and Lee are in error. Consequently, the drag coefficient given by Patel

$x_0/L$	$u_e$ exper.	H exper.	$\theta \times 10^4$ exper.	$\theta \times 10^4$ calc.(1)	$\theta \times 10^4$ calc.(2)
1.04	0.9690	1.319	1.509	1.509	1.521
1.06	0.9726	1.305	1.464	1.491	1.497
1.10	0.9803	1.279	1.361	1.453	1.446
1.20	0.9899	1.262	1.291	1.407	1.402
1.30	0.9915	1.235	1.197	1.400	1.390
1.40	0.9965	1.222	1.158	1.377	1.375
2.47	0.9999	1.124	1.007	1.362	-----
$\infty$	1.0000	1.000	-----	1.361	1.354

1 - Momentum equation with experimental H and  $u_e$ .

2 - Present strong interaction method.

Table 3. Variation of Wake Integral Parameters for F-57 Body.

and Lee (based on maximum frontal area) is too low. In fact their value, based on the measured  $\theta$  at  $x_0 = 2.47$ , is incorrect. They give  $C_D = 0.0092$  whereas it should be 0.0294. The present calculation gives  $C_D = 0.0396$ .

The large trip wire used in the experiment (1.664 mm in diameter) is responsible for the measured values of  $C_f$ , shown in Fig. 19, being considerably higher than the computed curve immediately downstream of the transition region. Beyond about  $x_0 = 0.70$  the effect of the wire dies out and the two calculated curves agree well with experiment. The trip wire also manifests itself in the shape factor distribution as shown in Fig. 20. Over the last 20 percent of body length the present calculation is too low but agrees well with experiment in the wake. The cause of the low  $H$  prediction on the aft end of the body is the algebraic turbulence model, as in the previous two cases. The shape factor is predicted by the present method more accurately for a concave tail than a convex one. The velocity profiles, shown in Figs. 21 - 23, illustrate respectively the trip wire effect near the wall at  $x_0 = 0.601$ , the usual overprediction of the velocity near the wall at  $x_0 = 0.88$  and a spurious bump near the wall in the calculated profile at  $x_0 = 0.99$  caused by extreme stretching of the normal step size from the Mangler transformation singularity at the tail.

6. Conclusions

The pressure mapping hypothesis of Weinbaum has been found to provide a simple means of adapting the displacement body concept to simulate streamline curvature effects in the high Reynolds number axisymmetric strong interaction problem. Calculated results by the present method for the three cases considered generally agree well with experiment except for the boundary-layer shape factor. The predictions by the present method, where a finite difference boundary-layer solution is used, are about the same in accuracy as the predictions of a good integral boundary-layer procedure such as that of Patel [17], except for the boundary-layer shape factor which is predicted better by the integral method. The reason for the poor prediction of  $H$  in the tail region by the present method is the basic inadequacy of an algebraic turbulence model in that region. Such a model does not properly represent the change from a boundary-layer profile to a wake profile nor does it include streamline curvature effects. The inadequacy of algebraic turbulence models in this regard has been noted by other investigators [3, 14, 15, 18].

The present calculated results for body drag coefficient have been found to agree well with experiment and to be as good or better as other published calculated values, at least for the Lyon model A body and the modified spheroid tested by Patel et al. For the case of the low drag F-57 body some doubt exists as to the validity of the measured momentum deficit area in the wake. The simple integral method of Granville has been used to model the wake development and hence predict  $\theta_\infty$  which is sensitive to the initial value of  $u_e$  in the wake. By using Weinbaum's hypothesis  $u_e$  has been corrected to account for streamline curvature effects in the tail-near wake region so that the predicted value of  $\theta_\infty$ , and hence  $C_D$ , is reasonably accurate.

Improvements in the present calculation method could be made in the following areas, in addition to modifying the turbulence model:

1. The approximation of concentric streamlines, Eq. (9), which leads to the simple form of Weinbaum's hypothesis, could be changed to a more realistic assumption. The resulting expression for the pressure change across the boundary layer would undoubtedly lead to a pressure mapping more complicated than that of Weinbaum.
2. The boundary-layer equations could be integrated in finite difference form downstream in the wake, as well as along the body, to eliminate the incompatibility of a finite difference solution with an integral solution. As long as boundary-layer coordinates are retained, this approach would work properly only for a body with a cusped tail. For a body with a nonzero tail angle boundary-layer coordinates do not mesh properly with cylindrical wake coordinates resulting in an overlap region in the coordinate systems. To restart the numerical calculation in the wake would require interpolation of the boundary-layer solution. Such an interpolation would not be satisfactory because the boundary-layer approximation is coordinate system dependent. In addition, the Cebeci-Smith boundary-layer scheme cannot be used in the wake because of the singularity at zero radius in the Mangler transformation. Physical coordinates should be used for a finite difference wake calculation.

One possibility of overcoming the coordinate mismatch problem at the tail-wake juncture is to abandon the usual boundary-layer coordinate system and use either a conformal system or a skewed system. At this stage the artificial division of the flow into a boundary layer and an outer inviscid region hardly seems worthwhile. In the new coordinates just mentioned one could proceed to a parabolized form of the Navier-Stokes equations, with an appropriate turbulence model, to be solved iteratively for the entire strong interaction region similar to the scheme of Schetz and Favin [2]. If done properly the machine time required to solve such a system should be little greater than the strong interaction procedure described herein. Such an alternative is presently under investigation.

References

- [1] T. T. Huang, H. T. Wang, N. Santelli and N. C. Groves, "Propellor/Stern/Boundary-Layer Interaction on Axisymmetric Bodies: Theory and Experiment," David W. Taylor Naval Ship Research and Development Center Report 76-0113, December 1976.
- [2] J. A. Schetz and S. Favin, "Numerical Solution for the Near Wake of a Body with Propeller," *J. Hydronautics* 11, 136 (1977).
- [3] G. Dyne, "A Streamline Curvature Method for Calculating the Viscous Flow Around Bodies of Revolution," *Internat. Symp. on Ship Viscous Resistance, Goteborg, Sweden* (1978).
- [4] S. Weinbaum, M. S. Kolansky, M. J. Gluckman and R. Pfeffer, "An Approximate Theory for Incompressible Viscous Flow Past Two-Dimensional Bluff Bodies in the Intermediate Reynolds Number Regime  $0(1) < Re < 0(10^2)$ ," *J. Fluid Mech.* 77, 129 (1976).
- [5] D. F. Myring, "The Profile Drag of Bodies of Revolution in Subsonic Flow," Royal Aircraft Establishment Tech. Report 72234 (1972).
- [6] T. D. Beatty, "A Theoretical Method for Analysis and Design of Axisymmetric Bodies," NASA CR-2498 (1975).
- [7] J. L. Hess and A.M.O. Smith, "Calculation of Potential Flow about Arbitrary Bodies," in Progress in Aeronautical Sciences, Vol. 8 (Pergamon Press, New York, 1966), Chapter 1.
- [8] T. Cebici and A.M.O. Smith, Analysis of Turbulent Boundary Layers (Academic Press, New York, 1974).
- [9] M. E. Crawford and W. M. Kays, "STAN5 - A Program for Numerical Computation of Two-Dimensional Internal and External Boundary Layer Flows", NASA CR-2742 (1976).
- [10] A. Nakayama, V. C. Patel and L. Landweber, "Flow Interaction Near the Tail of a Body of Revolution, Parts I and II", *J. Fluids Engin.* 98, 531 (1976).
- [11] P. S. Granville, "The Calculation of Viscous Drag of Bodies of Revolution", David Taylor Model Basin Report 849 (1953).
- [12] V. C. Patel and O. Guven, "Importance of the Near Wake in Drag Prediction of Bodies of Revolution", *AIAA J.* 14, 1132 (1976).
- [13] H. M. Lyon, "A Study of the Flow in the Boundary Layer of Streamline Bodies", Aeronautical Research Committee, R&M No. 1622 (1934).
- [14] V. C. Patel, A. Nakayama and R. Damian, "Measurements in the Thick Axisymmetric Turbulent Boundary Layer Near the Tail of a Body of Revolution", *J. Fluid Mech.* 63, 345 (1974).

- [15] V. C. Patel and Y. T. Lee, "Thick Axisymmetric Turbulent Boundary Layer and Near Wake of a Low-Drag Body of Revolution," Iowa Institute of Hydraulic Research Report No. 210, December, 1977.
- [16] K. K. Chen and N. A. Thyson, "Extension of Emmon's Spot Theory to Flows on Blunt Bodies", AIAA J. 5, 821 (1971).
- [17] V. C. Patel, "A Simple Integral Method for the Calculation of Thick Axisymmetric Turbulent Boundary Layers", Aeron. Quart. 25, 47 (1974).
- [18] T. T. Huang, N. Santelli and G. Belt, "Stern Boundary-Layer Flow on Axisymmetric Bodies," presented at Twelfth Symposium on Naval Hydrodynamics, Washington, DC, June 1978.

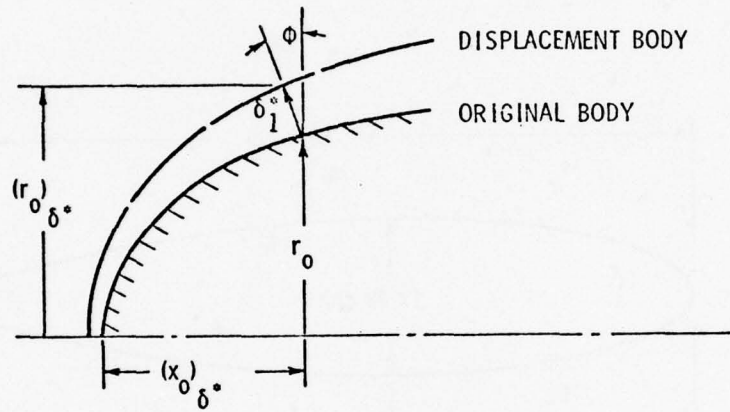


Figure 1. Displacement Body Geometry

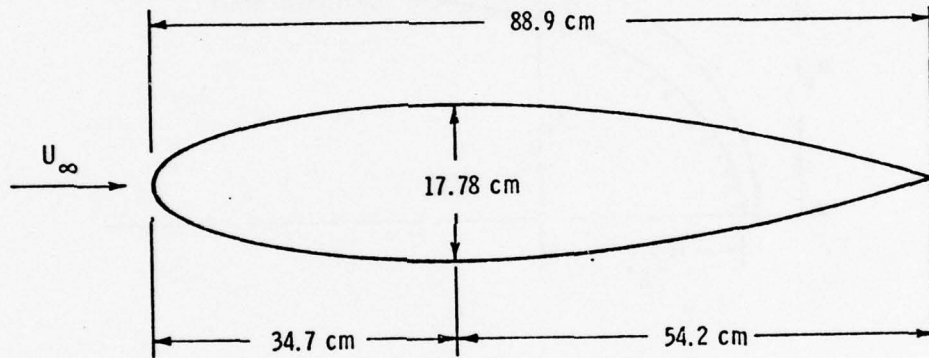


Figure 2. Lyon Model A Body Geometry

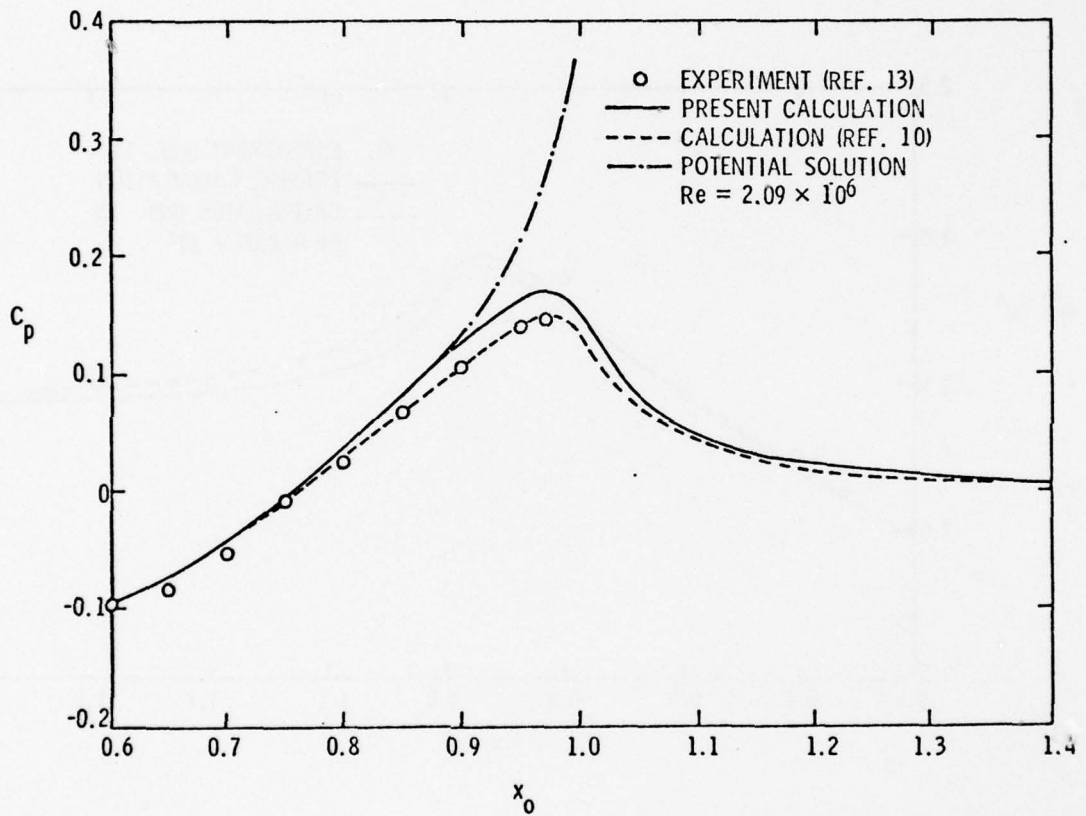


Figure 3. Pressure Distribution on Lyon Model A Body

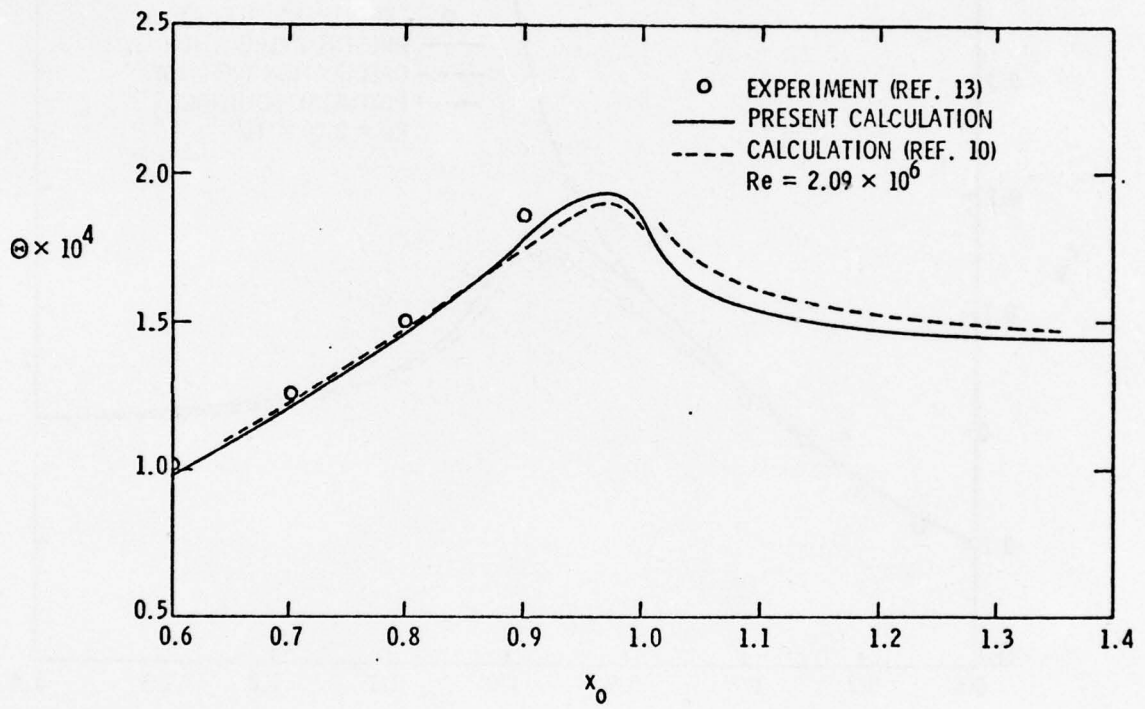


Figure 4. Momentum Deficit Area, Lyon Model A Body

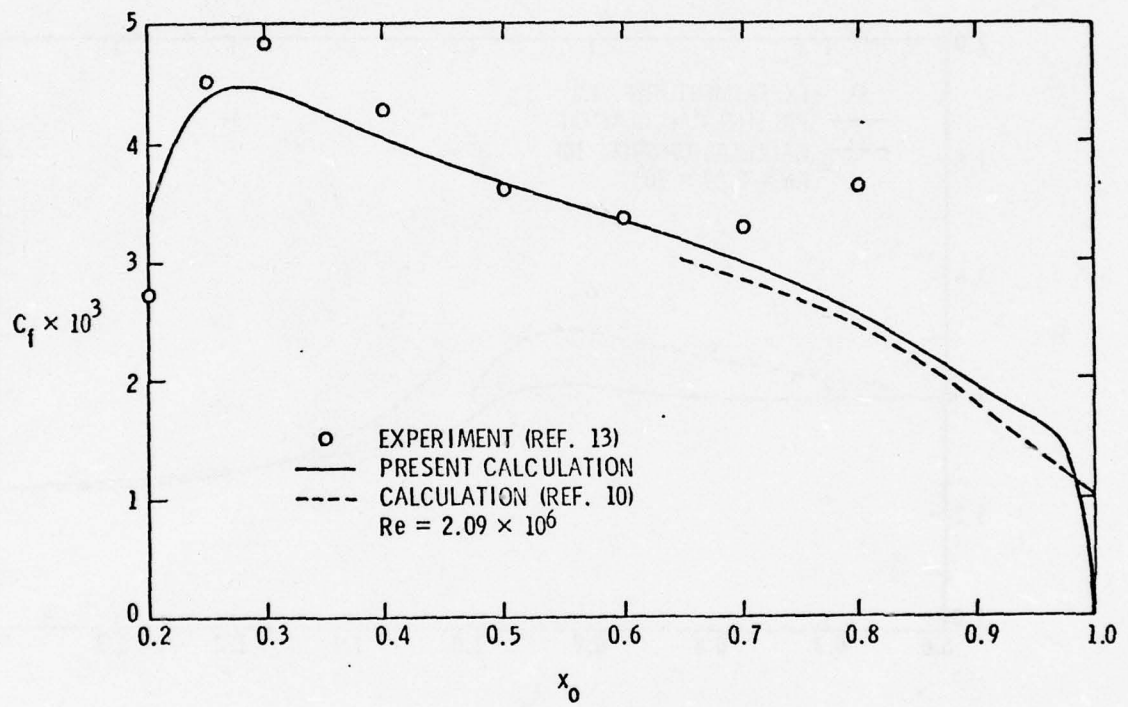


Figure 5. Wall Friction Coefficient, Lyon Model A Body

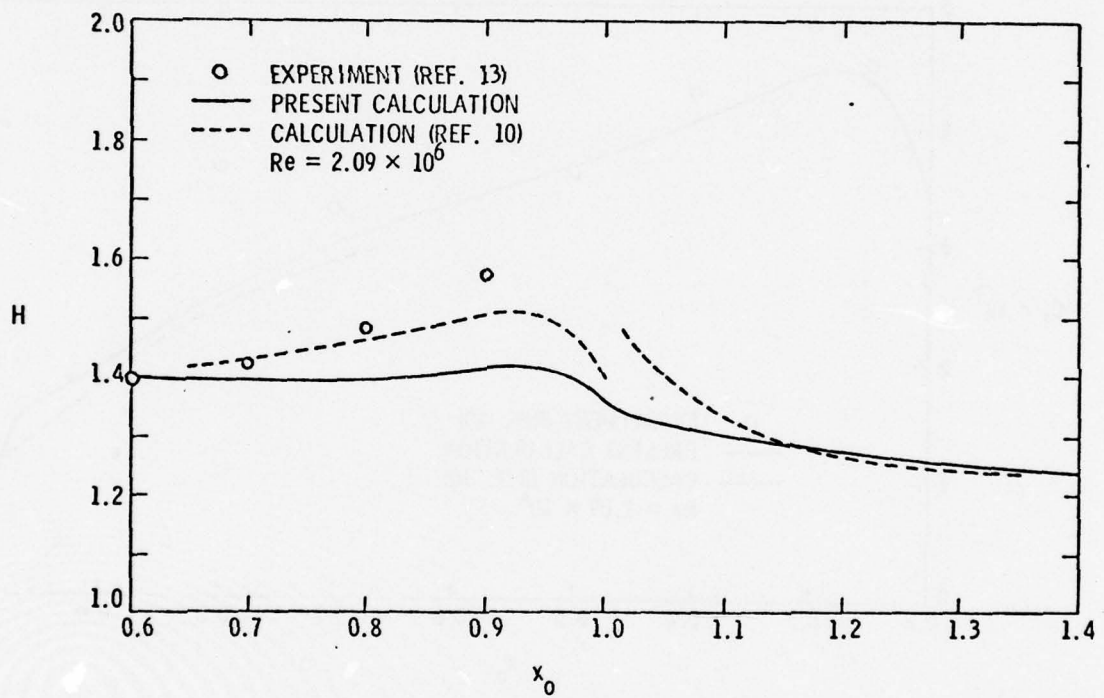


Figure 6. Boundary-Layer Shape Factor, Lyon Model A Body

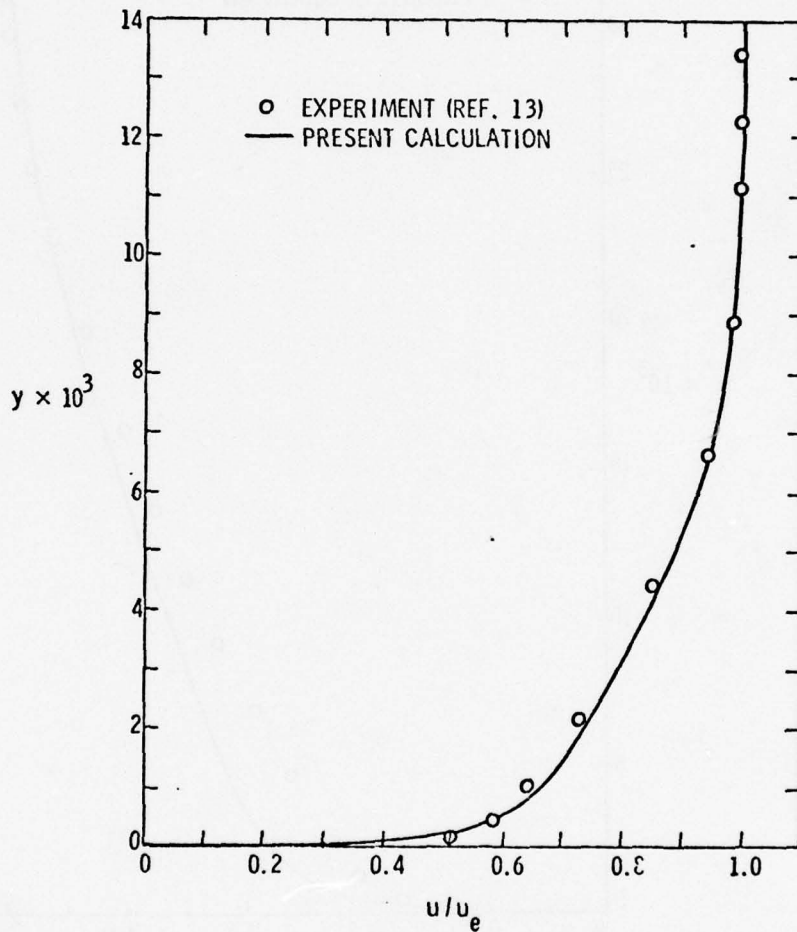


Figure 7. Mean Velocity Profile at  $x_0=0.60$ , Lyon Model A Body

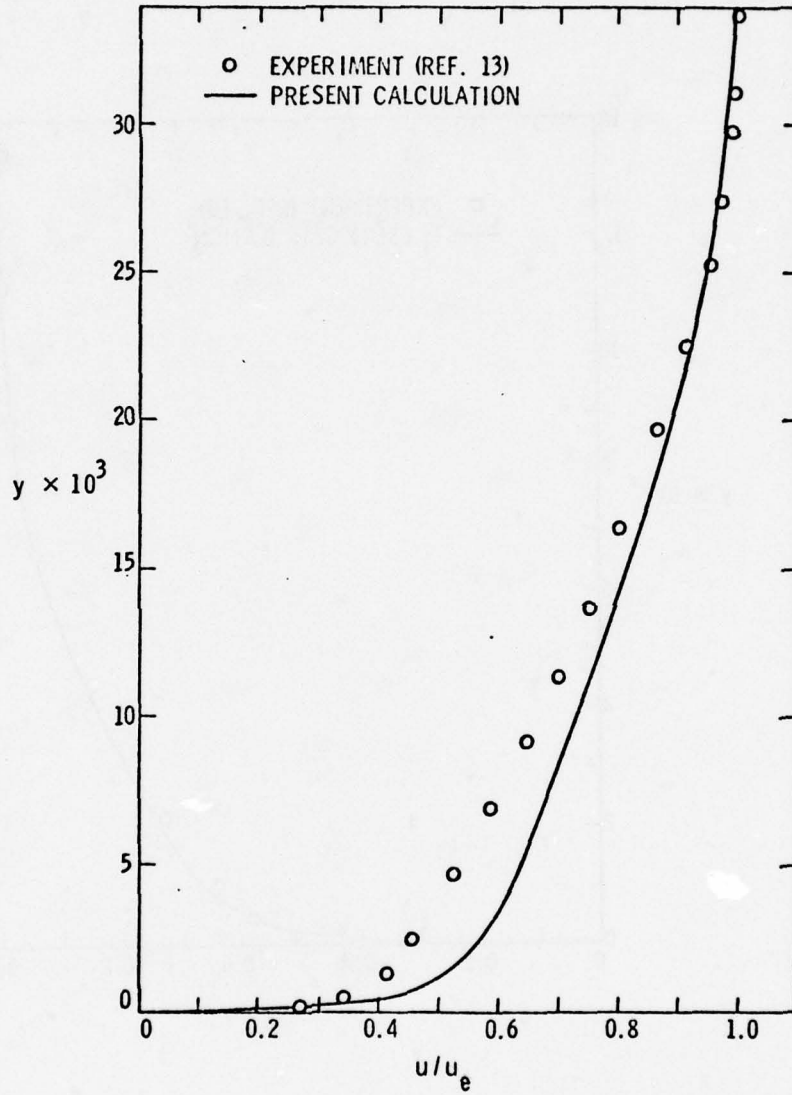


Figure 8. Mean Velocity Profile at  $x_0=0.90$ , Lyon Model A Body

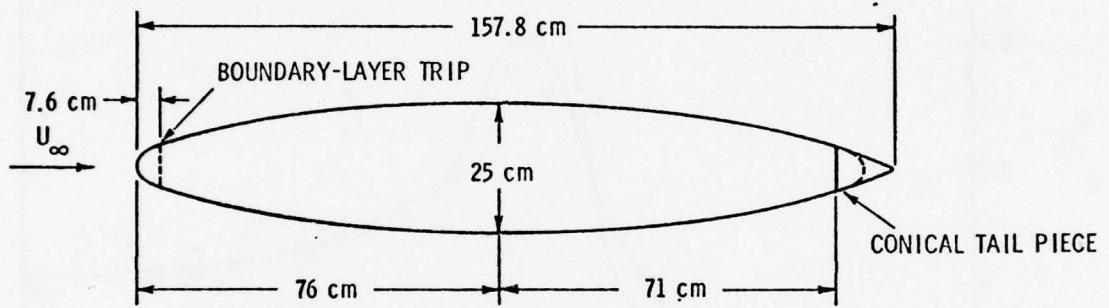


Figure 9. Modified Spheroid Geometry

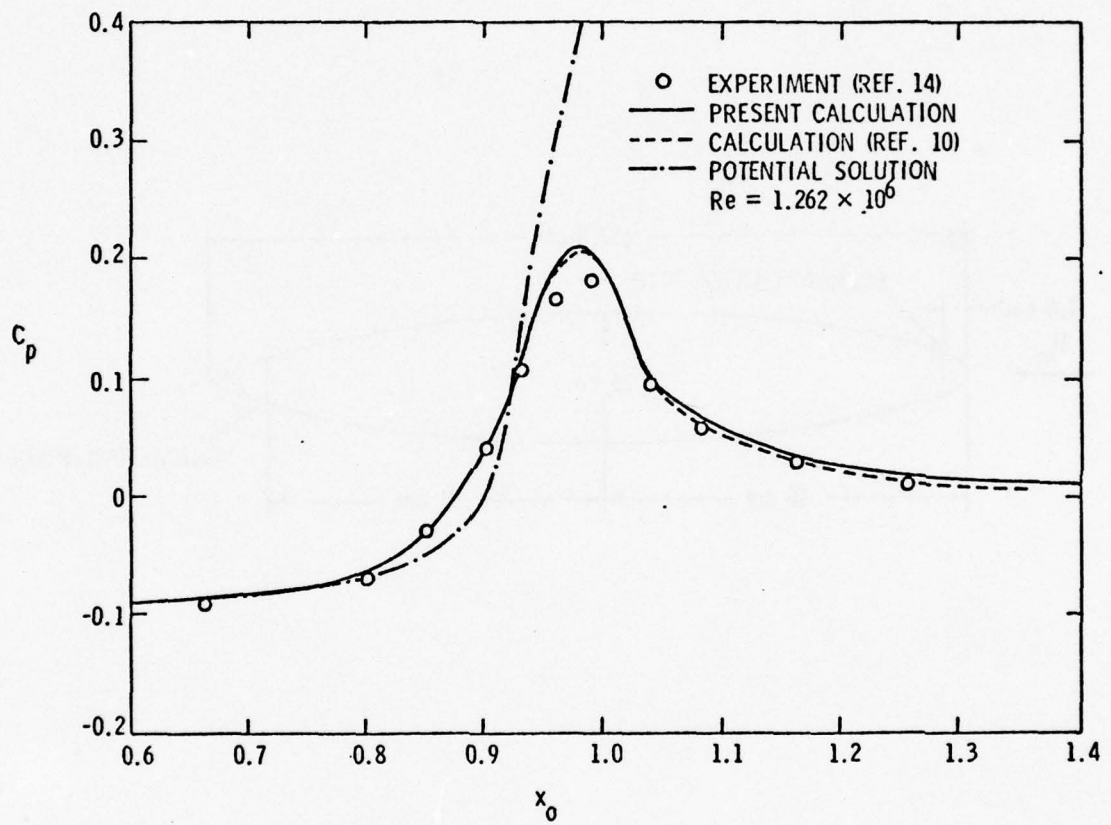


Figure 10. Pressure Distribution on Modified Spheroid

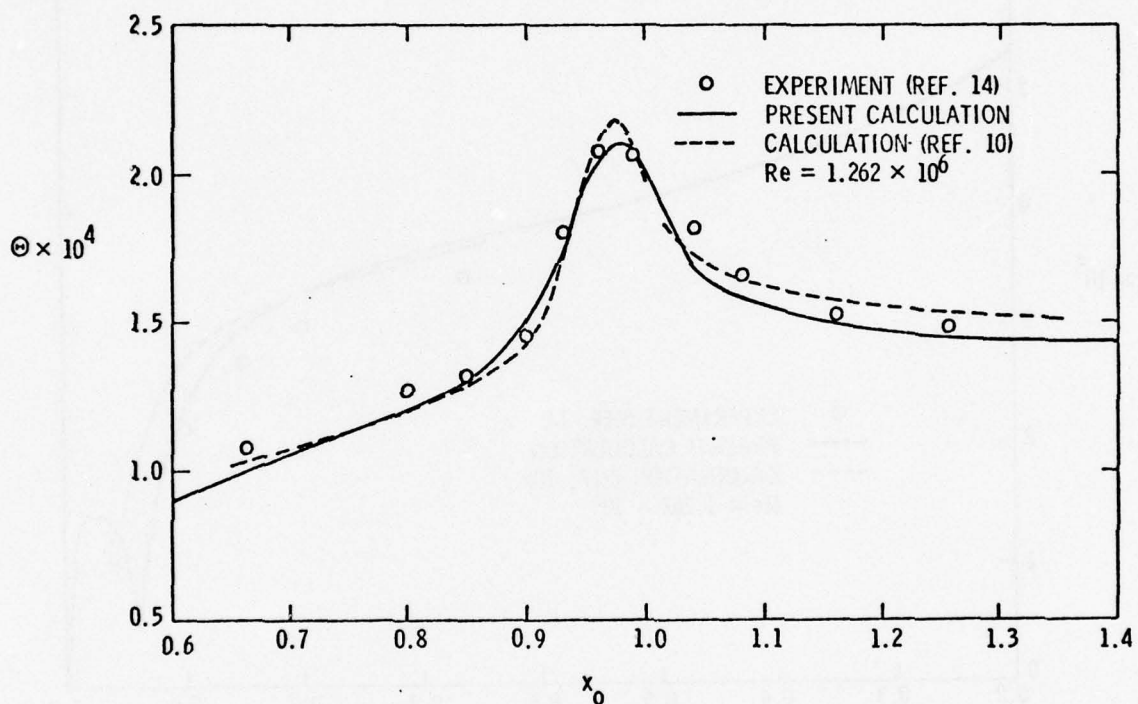


Figure 11. Momentum Deficit Area, Modified Spheroid

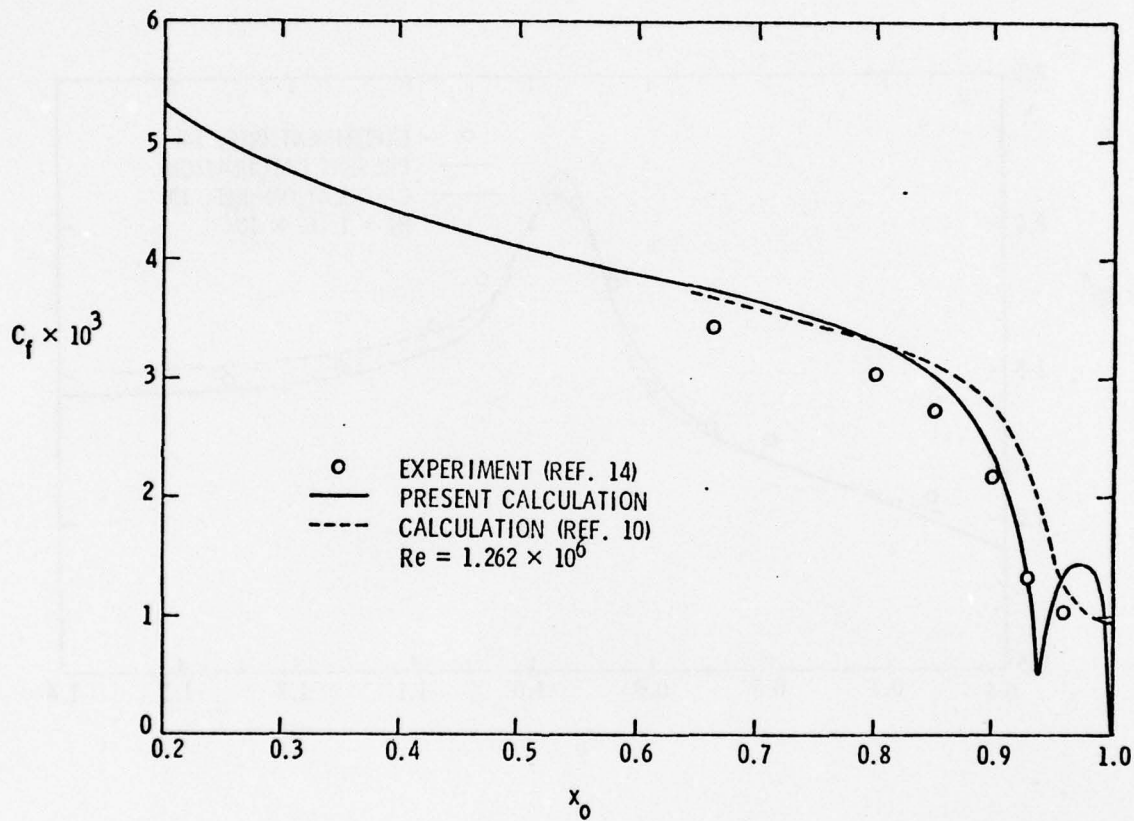


Figure 12. Wall Friction Coefficient, Modified Spheroid

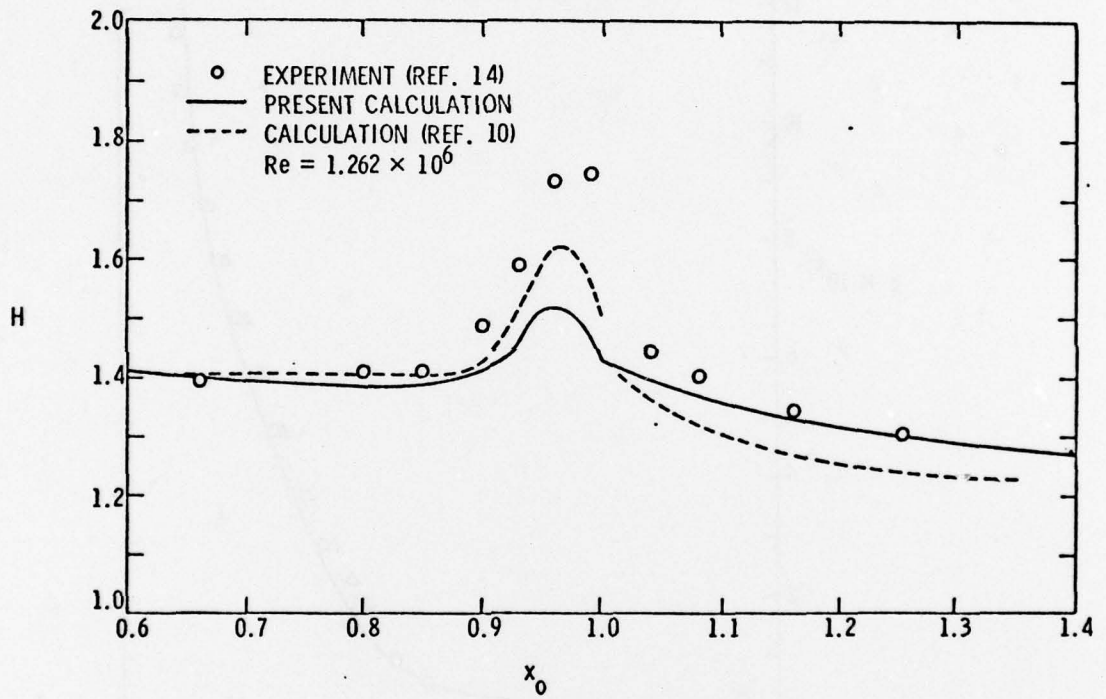


Figure 13. Boundary-Layer Shape Factor, Modified Spheroid

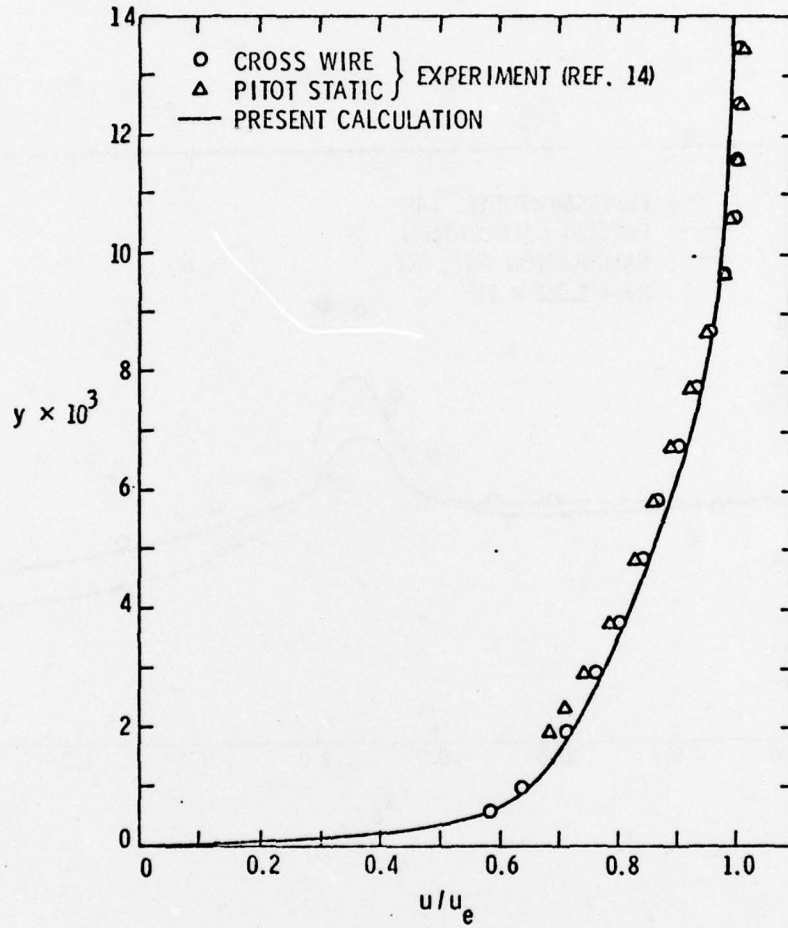


Figure 14. Mean Velocity Profile at  $x_0=0.662$ , Modified Spheroid

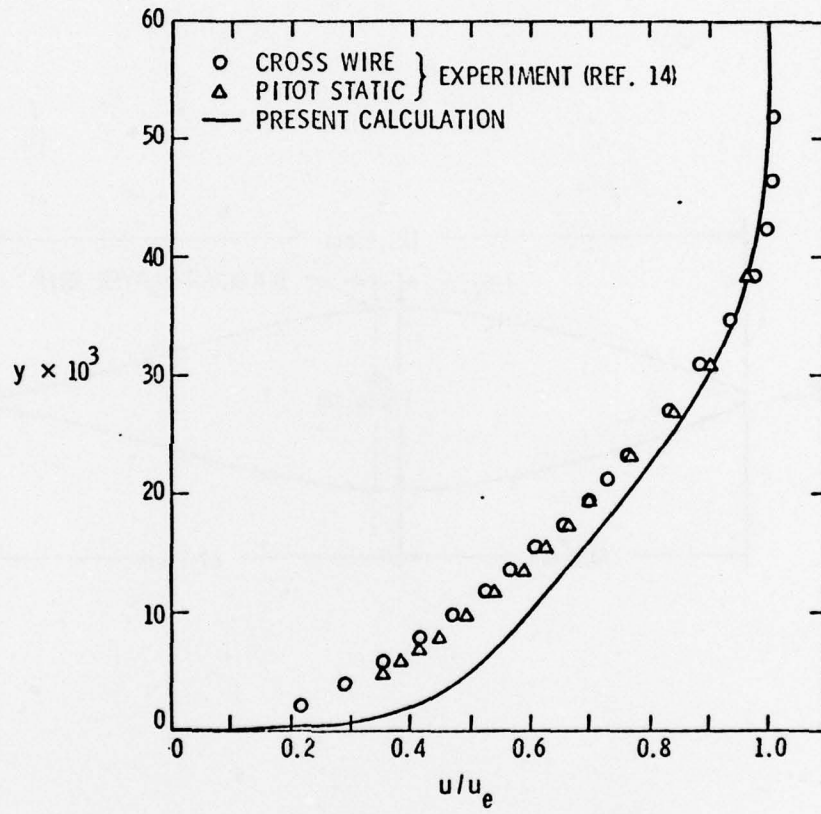


Figure 15. Mean Velocity Profile at  $x_0=0.96$ , Modified Spheroid

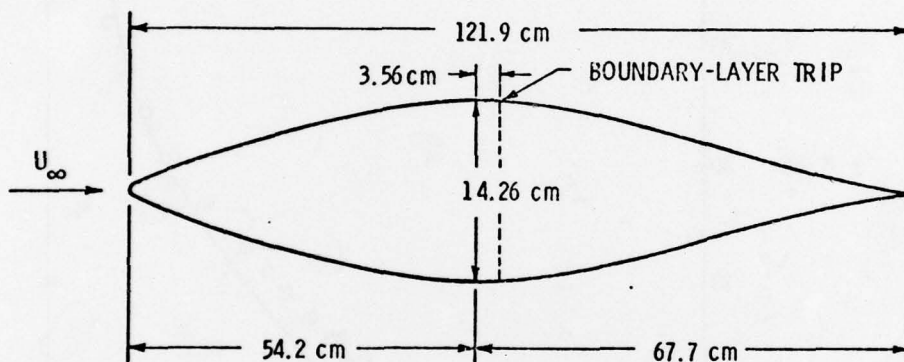


Figure 16. F-57 Body Geometry

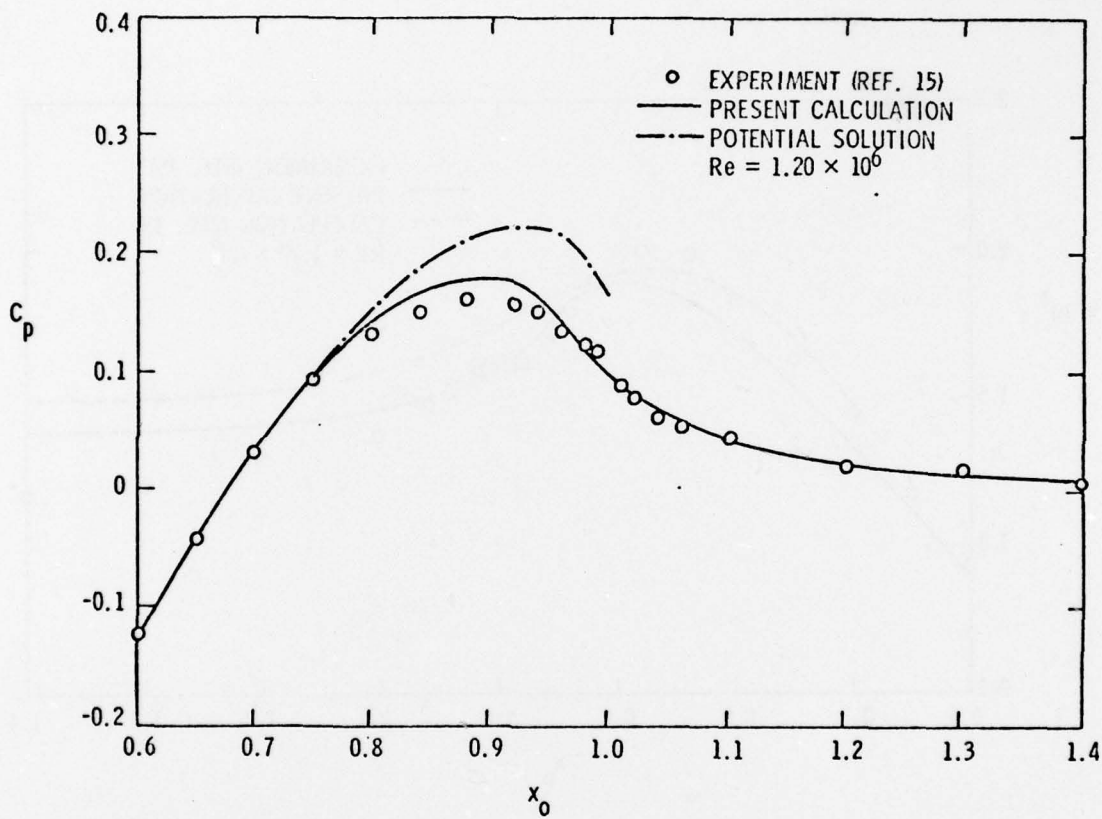


Figure 17. Pressure Distribution on F-57 Body

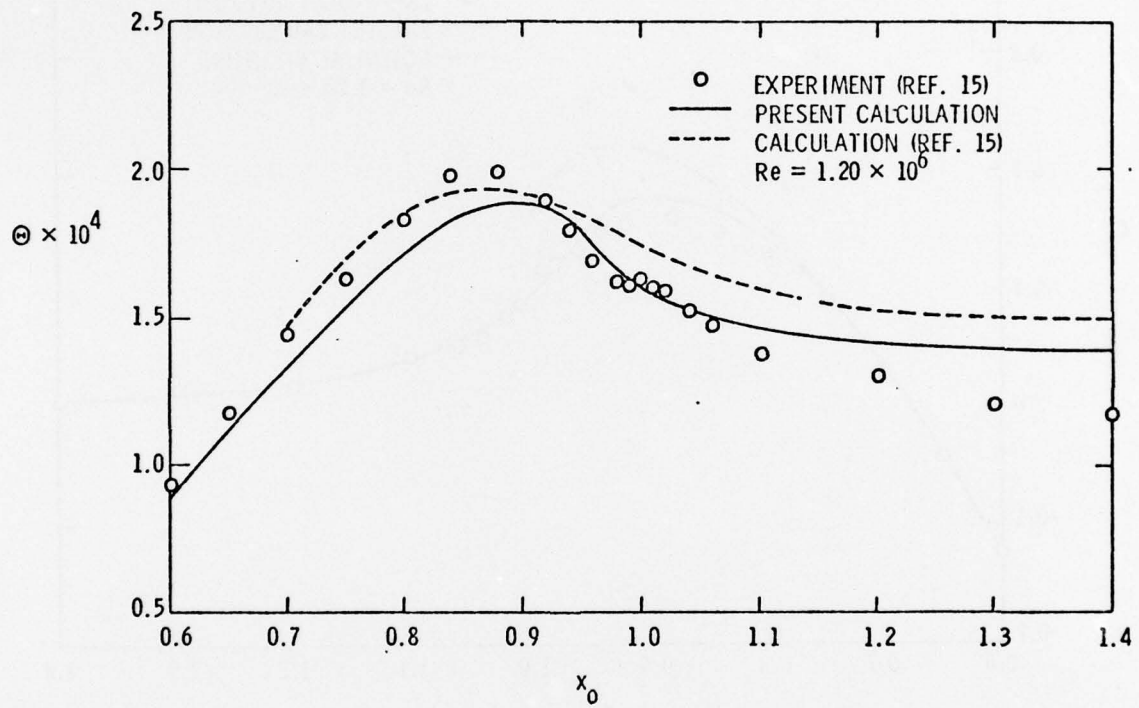


Figure 18. Momentum Area Deficit, F-57 Body

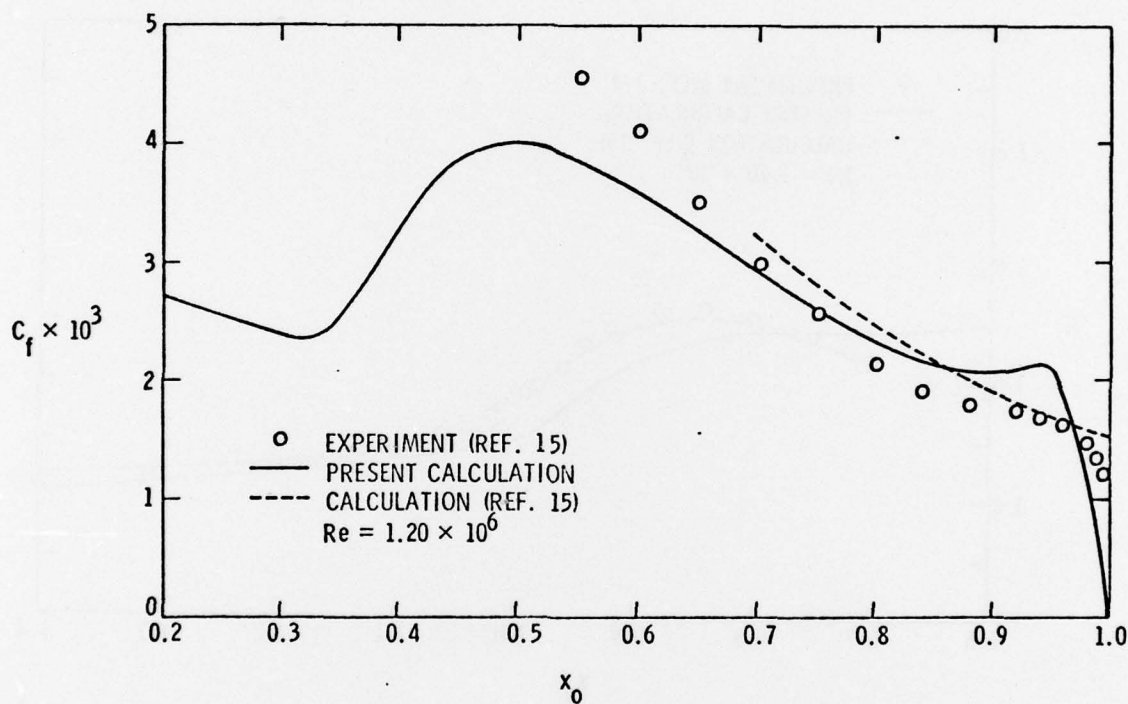


Figure 19. Wall Friction Coefficient, F-57 Body

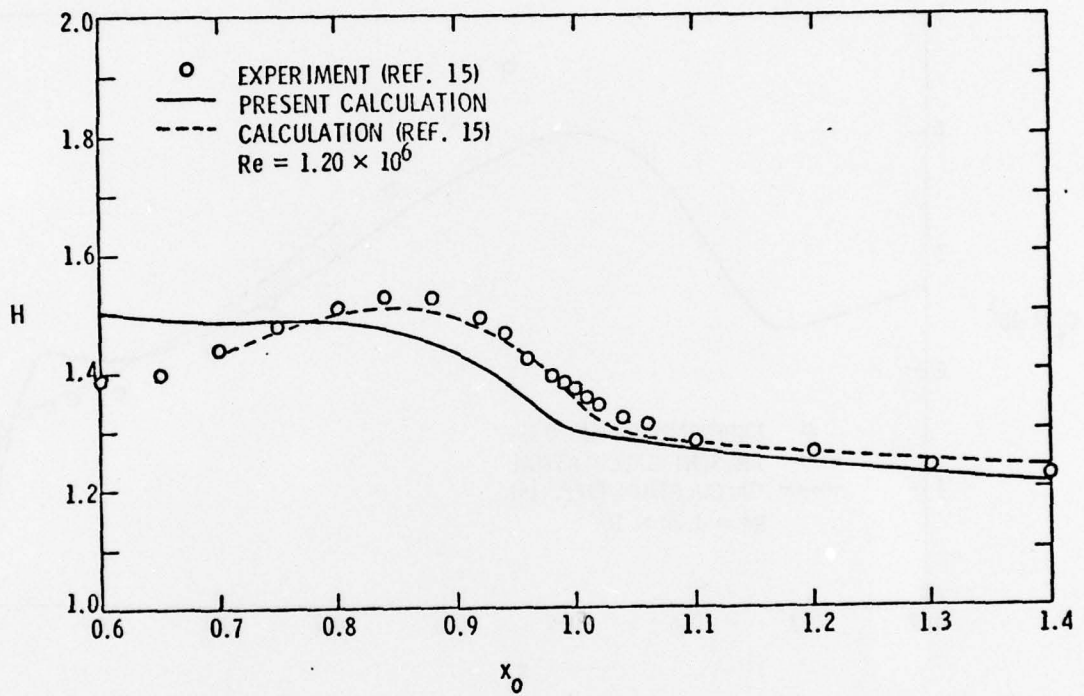


Figure 20. Boundary-Layer Shape Factor, F-57 Body

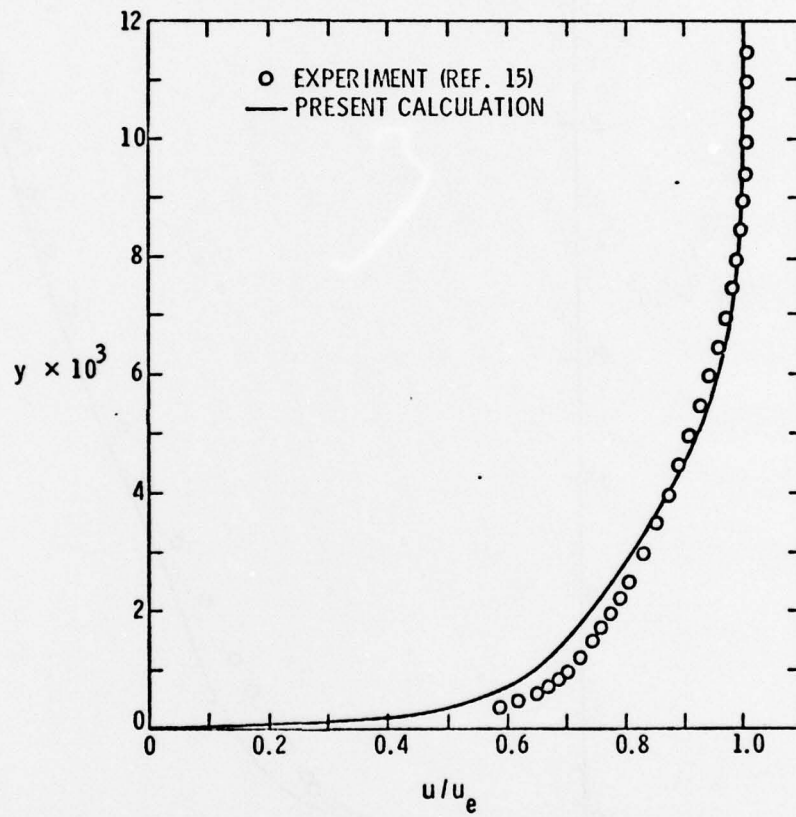


Figure 21. Mean Velocity Profile at  $x_0=0.601$ , F-57 Body

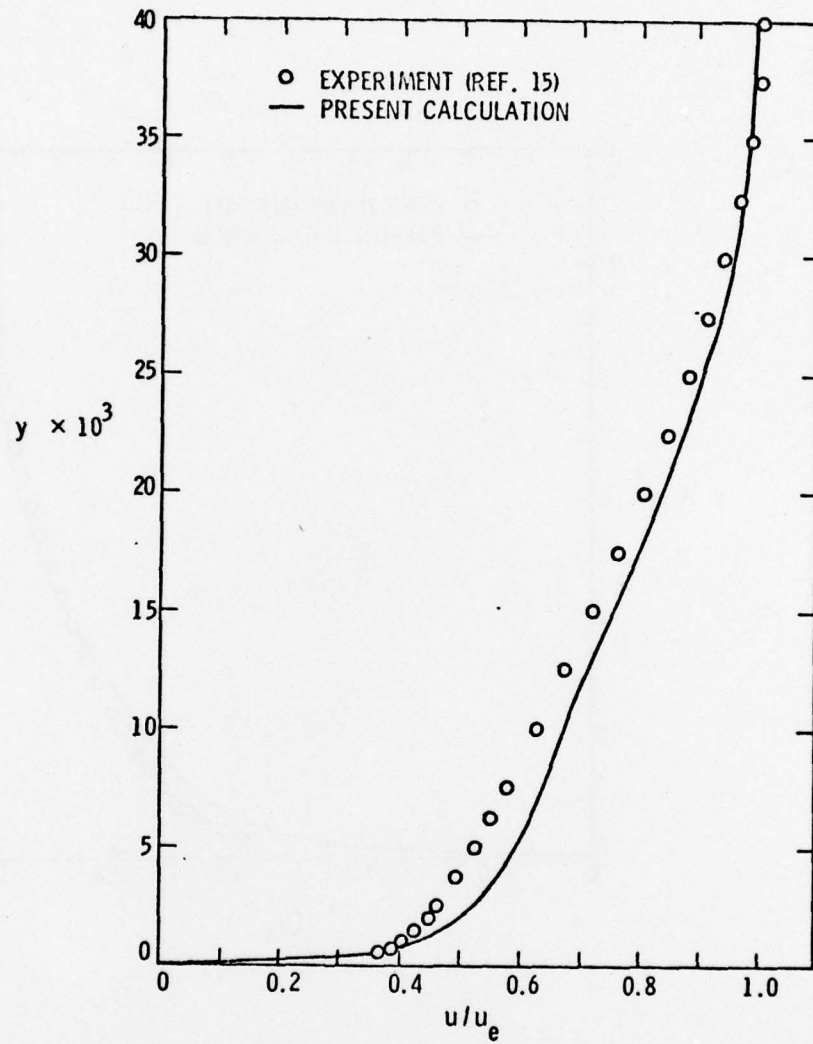


Figure 22. Mean Velocity Profile at  $x_0 = 0.880$ , F-57 Body

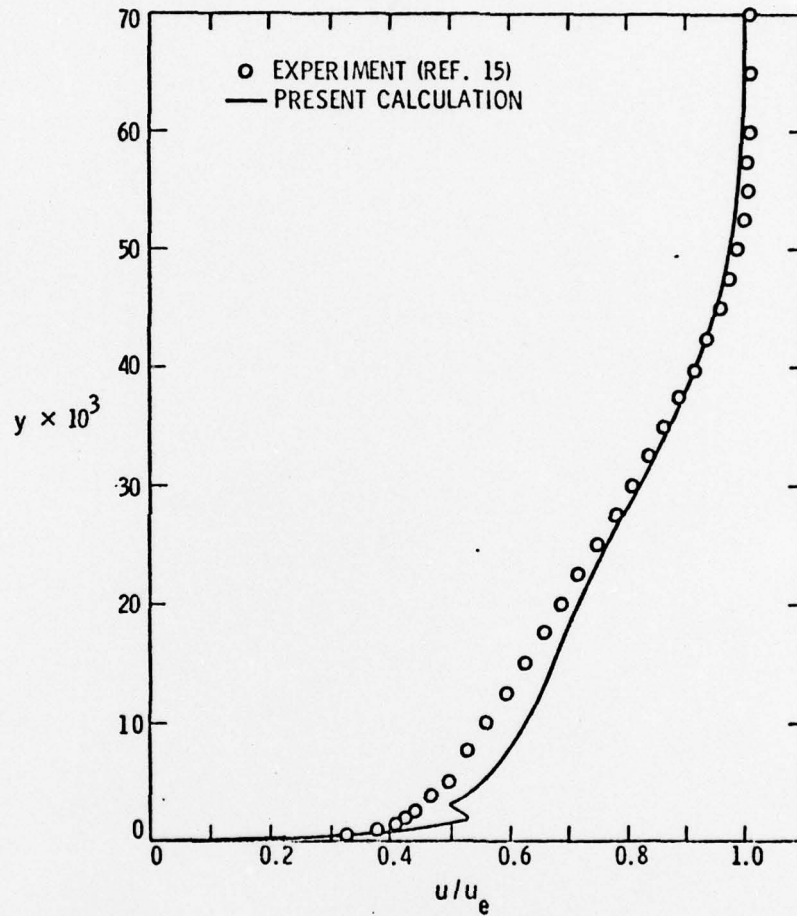


Figure 23. Mean Velocity Profile at  $x_0=0.990$ , F-57 Body

DISTRIBUTION LIST FOR UNCLASSIFIED TM 78-211 by G. H. Hoffman, dated July 19, 1978

Commander  
Naval Sea Systems Command  
Department of the Navy  
Washington, DC 20362  
Attn: Library  
Code NSEA-09G32  
(Copy No. 1 and 2)

Naval Sea Systems Command  
Attn: C. G. McGuigan  
Code NSEA-03133  
(Copy No. 3)

Naval Sea Systems Command  
Attn: L. Benen  
Code NSEA-0322  
(Copy No. 4)

Naval Sea Systems Command  
Attn: E. G. Liszka  
Code NSEA-0342  
(Copy No. 5)

Naval Sea Systems Command  
Attn: G. Sorokin  
Code NSEA-035  
(Copy No. 6)

Naval Sea Systems Command  
Attn: T. E. Peirce  
Code NSEA-0351  
(Copy No. 7)

Naval Sea Systems Command  
Attn: J. G. Juergens  
Code NSEA-037  
(Copy No. 8)

Naval Sea Systems Command  
Attn: H. C. Claybourne  
Code NSEA-0371  
(Copy No. 9)

Naval Sea Systems Command  
Attn: A. R. Paladino  
Code NSEA-0372  
(Copy No. 10)

Commander  
Naval Ship Engineering Center  
Department of the Navy  
Washington, DC 20360  
Attn: F. Welling  
Code NSEC-6144  
(Copy No. 11)

Commanding Officer  
Naval Underwater Systems Center  
Newport, RI 02840  
Attn: C. N. Pryor  
Code 01  
(Copy No. 12)

Naval Underwater Systems Center  
Attn: D. Goodrich  
Code 36315  
(Copy No. 13)

Naval Underwater Systems Center  
Attn: R. Nadolink  
Code 36315  
(Copy No. 14)

Naval Underwater Systems Center  
Attn: R. Trainor  
Code 36314  
(Copy No. 15)

Naval Underwater Systems Center  
Attn: F. White  
Code 36301  
(Copy No. 16)

Naval Underwater Systems Center  
Attn: Library  
Code 54  
(Copy No. 17)

Commanding Officer  
Naval Ocean Systems Center  
San Diego, CA 92152  
Attn: J. W. Hoyt  
Code 2501  
(Copy No. 18)

Naval Ocean Systems Center  
Attn: D. Nelson  
Code 2542  
(Copy No. 19)

Naval Ocean Systems Center  
Attn: A. G. Fabula  
Code 5311  
(Copy No. 20)

DISTRIBUTION LIST FOR UNCLASSIFIED TM 78-211 by G. H. Hoffman, dated July 19, 1978

Commanding Officer and Director  
David W. Taylor Naval Ship R&D Center  
Department of the Navy  
Bethesda, MD 20084  
Attn: W. E. Cummins  
Code 15  
(Copy No. 21)

David W. Taylor Naval Ship R&D Center  
Attn: S. F. Crump  
Code 1505  
(Copy No. 22)

David W. Taylor Naval Ship R&D Center  
Attn: W. B. Morgan  
Code 154  
(Copy No. 23)

David W. Taylor Naval Ship R&D Center  
Attn: R. Cumming  
Code 1544  
(Copy No. 24)

David W. Taylor Naval Ship R&D Center  
Attn: T. Huang  
Code 1552  
(Copy No. 25)

David W. Taylor Naval Ship R&D Center  
Attn: J. McCarthy  
Code 1552  
(Copy No. 26)

David W. Taylor Naval Ship R&D Center  
Attn: M. Sevik  
Code 19  
(Copy No. 27)

David W. Taylor Naval Ship R&D Center  
Attn: Library  
Code 522  
(Copy No. 28)

Commanding Officer and Director  
David W. Taylor Naval Ship R&D Center  
Department of the Navy  
Annapolis Laboratory  
Annapolis, MD 21402  
Attn: J. G. Stricker  
Code 2721  
(Copy No. 29)

Commander  
Naval Surface Weapon Center  
Silver Spring, MD 20910  
Attn: G. C. Gaunaurd  
Code R-31  
(Copy No. 30)

Naval Surface Weapon Center  
Attn: J. L. Baldwin  
Code WA-42  
(Copy No. 31)

Naval Surface Weapon Center  
Attn: W. J. Glowacki  
Code R-44  
(Copy No. 32)

Office of Naval Research  
Department of the Navy  
800 N. Quincy Street  
Arlington, VA 22217  
Attn: R. Cooper  
Code 438  
(Copy No. 33)

Office of Naval Research  
Attn: H. Fitzpatrick  
Code 438  
(Copy No. 34)

Defense Documentation Center  
5010 Duke Street  
Cameron Station  
Alexandria, Va 22314  
(Copies No. 35 to and including 46)

National Bureau of Standards  
Aerodynamics Section  
Washington, DC 20234  
Attn: P. S. Klebanoff  
(Copy No. 47)

Rand Corporation  
1700 Main Street  
Santa Monica, CA 90406  
Attn: R. King  
(Copy No. 48)

Rand Corporation  
Attn: C. Gazley  
(Copy No. 49)

DISTRIBUTION LIST FOR UNCLASSIFIED TM 78-211 by G. H. Hoffman, dated  
July 19, 1978

Jet Propulsion Laboratory  
4800 Oak Grove Drive  
Pasadena, CA 91103  
Attn: Dr. Leslie Mack  
(Copy No. 50)

Iowa Institute of Hydraulic Research  
The University of Iowa  
Iowa City, Iowa 52240  
Attn: V. C. Patel  
(Copy No. 51)

Dynamics Technology, Inc.  
3838 Carson Street, Suite 110  
Torrance, CA 90503  
Attn: Wayne H. Haigh  
(Copy No. 52)

Applied Research Laboratory  
The Pennsylvania State University  
Post Office Box 30  
State College, PA 16801  
Attn: J. J. Eisenhuth  
(Copy No. 53)

Applied Research Laboratory  
Attn: R. E. Henderson  
(Copy No. 54)

Applied Research Laboratory  
Attn: G. H. Hoffman  
(Copy No. 55)

Applied Research Laboratory  
Attn: B. E. Robbins  
(Copy No. 56)

Applied Research Laboratory  
Carfield Thomas Water Tunnel File  
(Copy No. 57)